PERGAMON

Journal of Structural Geology 23 (2001) 1393–1413

JOURNAL OF STRUCTURAL GEOLOGY

www.elsevier.com/locate/jstrugeo

Rheological and microstructural evolution of Carrara marble with high shear strain: results from high temperature torsion experiments

Marco Pieri[a], Luigi Burlini[a], Karsten Kunze[a,*], Iona Stretton[b], David L. Olgaard[c]

[a]*Geologisches Institut, Eidgenössische Technische Hochschule, ETH-Zentrum, CH-8092 Zürich, Switzerland*
[b]*Bayerisches Geoinstitut, Universität Bayreuth, D-95440 Bayreuth, Germany*
[c]*ExxonMobil Upstream Research Company, P.O. Box 2189, Houston, TX 77252, USA*

Received 4 October 1999; accepted 19 December 2000

Abstract

This study investigated the rheological and microstructural evolution of Carrara marble deformed to large shear strain to understand how dynamic recrystallization and lattice-preferred orientation (LPO) are related to strain softening processes. Solid cylinders of Carrara marble were deformed in torsion up to a shear strain of $\gamma = 11$ at constant twist rates, which correspond to a shear strain rate of 3×10^{-4} s^{-1} at the outer surface, and at temperatures of 1000 and 1200 K (727 and 927°C, respectively). For the initial grain size of 150 μm, these conditions are within the dislocation creep regime.

Substantial changes in both rheology and microstructure were observed as the marble deformed to high shear strain at 1000 K (1200 K). A peak stress was reached at about $\gamma = 1$ ($\gamma = 0.5$) followed by moderate strain weakening. An apparent steady-state flow stress was obtained at high shear strain of $\gamma > 5$ ($\gamma > 2$). The stress exponent n decreased slowly with strain from 10 ($\gamma = 1$) to 6 ($\gamma = 9$) at 1000 K, but it remained approximately constant at 1200 K (n around 10). At the maximum reached shear strain of $\gamma = 11$ ($\gamma = 8.5$), the marble had almost completely recrystallized to a fine grain size of about 10 μm (20 μm). A secondary foliation developed in the recrystallized matrix, which is at a large oblique angle to the shear zone boundary (SZB). LPO was measured by electron backscatter diffraction (EBSD). For both temperatures, the LPO evolved from an oblique deformation texture to a very sharp and symmetric single orientation component with $r\{10\bar{1}4\}$ parallel to the shear plane and $a\langle\bar{1}2\bar{1}0\rangle$ parallel to the shear direction. It is concluded that strain weakening was associated with the development of a strong LPO during dynamic recrystallization to a finer grain size. Mechanical and microstructural steady-state is only reached at large shear strain. The steady-state lattice and grain shape fabrics can hardly be used as shear sense indicators in such recrystallized calcite mylonites.

1. Introduction

Attempts to model lithospheric deformation are usually based on experimentally generated flow laws. Studies that have generated descriptions of the flow behavior of rocks at high temperatures have typically assumed that a steady-state distributed flow develops after an initial transient creep period under constant stress, temperature and strain rate and that this steady-state continues indefinitely. In naturally deformed rocks, however, flow commonly localizes at high strain into shear zones, which are microstructurally very different from their protolith (e.g. Etheridge and Wilkie, 1979). By implication, strength characteristics must also evolve progressively during large plastic strain increments (Rutter, 1999). The plastic deformation mechanisms by which strength characteristics evolve include: (a) a switch in deformation mechanism from dislocation creep to grain size sensitive flow (Schmid et al., 1977); (b) waves of recrystallization replacing the strained crystals with dislocation free grains (Tullis and Yund, 1982); and (c) geometrical softening where easy slip systems align favorably for the macroscopic shear (White et al., 1980; Schmid, 1982; Urai et al., 1986).

Geological deformation is commonly non-coaxial, i.e. the axes of finite strain rotate during successive strain increments. Most rock deformation experiments were performed under uni-axial compression, however. Non-coaxial experiments have been performed to relatively high shear strains ($\gamma \leq 3$) using a diagonal saw cut assembly in an axial compression apparatus on monomineralic aggregates of calcite, olivine and quartz (Schmid et al., 1987; Zhang and Karato, 1995; Dell Angelo and Tullis, 1996). Although such experiments provide important information on textures and microstructures, lateral offsets complicate the derivation of accurate strength data at higher strain and of the

* Corresponding author. Tel.: +41-1-632-5695; fax: +41-1-632-1080.
E-mail address: kunze@erdw.ethz.ch (K. Kunze).

0191-8141/01/$ - see front matter
PII: S0191-8141(01)00006-2

actual deformation regime, which may contain a flattening strain component.

Torsion tests are often used in materials science, yet they have been used only rarely in experimental rock deformation (Handin et al., 1960, 1967; Casey et al., 1998; Paterson and Olgaard, 2000). Torsion is routinely used in experiments on organic analogs (Jessell and Lister, 1991; Bons and Jessell, 1999), in which similar micromechanisms to those operative in rocks are assumed to be active. The microstructural and textural evolution as a function of strain appears to closely approximate those which are inferred to occur in earth materials, but analog experiments do not provide relevant information on their rheology.

The rheology of calcite has been extensively investigated in the past, because it is an important geological mineral, does not react or change phase in the range of test conditions and deforms at lower temperatures than silicate rocks. Several regimes of plastic deformation have been distinguished (Schmid et al., 1977, 1980; Walker et al., 1990): twinning and intracrystalline glide regime (at low temperature and high differential stresses), grain size insensitive creep (at high temperature and high stress) and grain size sensitive creep (at high temperature and low stress). These regimes differ by rheological parameters and by the produced lattice-preferred orientations (LPOs, here also referred to as 'texture') and microstructures (Wenk et al., 1973; Schmid et al., 1980; Rutter et al., 1994). All the studies were based on experiments to a limited finite strain, in which neither mechanical nor microstructural steady-state might have been established.

It was inferred from uni-axial experiments on calcite aggregates to low strain (Rutter et al., 1994), that similar LPOs as those developing during crystal plastic deformation evolve somewhat slower through the broad transition into grain size sensitive flow, which was expected to occur as a consequence of grain refinement by dynamic recrystallization. This was interpreted to reflect an important role of intracrystalline plasticity in the accommodation of grain boundary sliding. Earlier formed textures survived even subsequent high-temperature deformation by power law or grain size sensitive flow, although the microstructures could be totally annealed.

High strain experiments were performed in uni-axial extension on Carrara marble (Rutter, 1998). Mechanical data were determined from a necked specimen in which a strain up to $\sim$1000% (corresponding to $\gamma \sim 10$) was observed. Steady-state flow stress was not achieved even at that strain and the microstructure continued to evolve with strain.

High strain ($\gamma < 20$) torsion experiments on fine grained Solnhofen limestone demonstrated that mechanical and microstructural steady-state establishes at high strain (Casey et al., 1998). Strain softening of about 10% occurred over a large strain interval. Even though the fine grained material was expected to deform dominantly by grain size sensitive flow, a stationary LPO of moderate strength established for shear strain $\gamma \geq 10$. This was interpreted as a result of strain partitioning between crystal plastic deformation and grain boundary sliding.

It was therefore of interest to extend such large strain studies to coarse-grained Carrara marble and to explore the rheology and the fabric evolution over a much larger strain range than previously accessible. The texture development of calcite by deformation and dynamic recrystallization was studied in samples from torsion experiments of Carrara marble at 1000 K (Pieri et al., 2001). Shear deformation produced first a deformation texture with monoclinic sample symmetry and an oblique *c*-axis distribution relative to the shear plane. With increasing shear, the marble recrystallized by subgrain rotation and nucleation of small grains. The LPO changed completely from the monoclinic deformation texture into a distribution with a sharp single orientation component with $r\{10\bar{1}4\}$ parallel to the shear plane and $a\langle\bar{1}2\bar{1}0\rangle$ parallel to the shear direction. Simple shear deformation of calcite was modeled with the self-consistent polycrystal plasticity theory including a model for dynamic recrystallization. The model results agree with experimental data if slip on $r\{10\bar{1}4\}$ $a\langle\bar{1}2\bar{1}0\rangle$ is introduced as a potential slip system for calcite. In that case, the steady-state recrystallization texture has an 'easy slip' preferred orientation.

This paper is intended to complement the textural study of Pieri et al. (2001) by a detailed rheological and microstructural analysis on two series of high strain torsion experiments of Carrara marble at 1000 and 1200 K, respectively. It describes how dynamic recrystallization and LPO are related to strain softening processes during high strain deformation.

2. The Carrara marble 'Lorano Bianco'

2.1. A marble laboratory standard

The Carrara marble used as the starting material in this study is called 'Lorano Bianco' because it is white marble collected from the Lorano quarry located approximately 8 km NNE of Carrara, Italy (Fig. 1a). A large block (2 m × 1 m × 1 m) of this marble was collected as a laboratory standard by D. Olgaard and M. Pieri (ETH, Zürich, Switzerland) and M. Coli (University of Florence, Italy). The perpendicular faces of the original block and of any sawed slabs or cubes were labeled A, B, and C, and oriented in geographical coordinates (Fig. 1b and c). Pieces of this block have been distributed to several laboratories to be used as a standard marble for rock testing.[1]

2.2. Stratigraphic and tectonic setting

Carrara marble is a lithostratigraphic formation of the

[1] Slabs or cubes (up to 50 kg) of this material are available on request through B. Evans (MIT, Cambridge, MA, USA) or J.-P. Burg (ETH, Zürich, Switzerland).

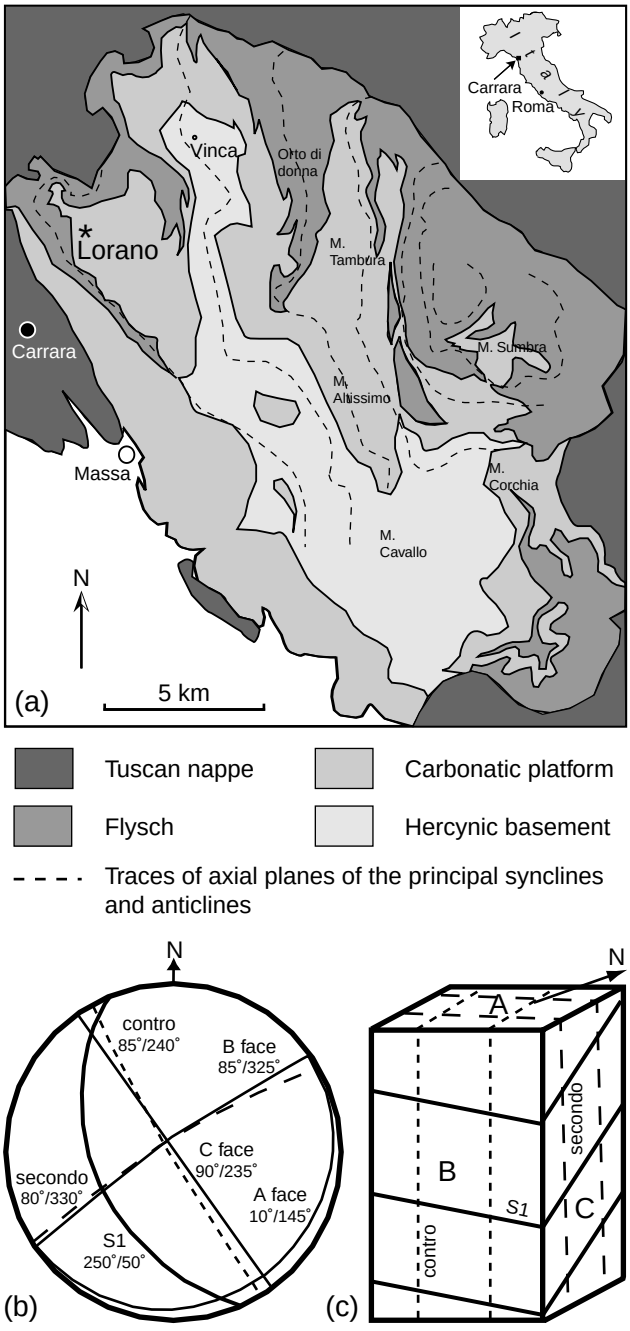

Fig. 1. Origin of the Carrara marble 'Lorano Bianco'. (a) Geological map of the Apuane Alps metamorphic complex (central Italy) simplified after Carmignani et al. (1978) with the location of the Lorano quarry indicated. (b) Orientation of the block faces A, B and C and the regional structural surfaces S_1 (main schistocity), secondo and contro. Lower hemisphere stereographic projection. (c) Schematic drawing of the sampled Lorano block with the structural surfaces.

Apuane Alps metamorphic complex exposed in a tectonic window below the Tuscan Nappe (Fig. 1a). It was subjected to three Tertiary deformation events under greenschist facies conditions (for details see, for example, Carmignani and Klingfield (1990); Coli (1989)). It is still under discussion whether, and how, these deformation phases are preserved in the marble (e.g. Molli et al., 2000).

Three structural elements were recognized in the Lorano quarry where the block was collected (Fig. 1b). The S_1 main schistosity called 'verso' is marked by bands of different gray colors as well as by thin dolomitic layers. Two systems of joints called 'secondo' and 'contro' are dipping very steeply at a right angle relative to each other.

2.3. Material characterization

Microscopic observations and element analysis by inductive-coupled plasma mass spectroscopy (ICP-MS, Table 1) showed that the calcite marble is extremely pure. The marble consists of 98% calcite with occasional grains of quartz, white mica, dolomite, epidote and pyrite. Light gray trails composed of very fine grained phyllosilicates are typical in this rock.

In cross-polarized light (Fig. 2a), grains show net extinction without any microscopic evidence of subgrains or strain features. Grain boundaries are usually straight, though sometimes slightly dentate to sutured. Some of the grains show very thin and straight twins. Triple point grain boundary intersections are approximately 120°, which is typical for statically recrystallized microstructures.

The two-dimensional grain size distribution (Fig. 2b) has an arithmetic average of about 150 μm. Texture and grain shape analysis showed that lattice- and shape-preferred orientations (SPOs), respectively, are very weak and that they are not related to any of the macroscopic structural surfaces (Fig. 2c and d). The observed directional variations are considered to be due to limited counting statistics in the measured population of grains at the sample surface.

Despite the three deformation phases under greenschist facies conditions known in this area, little evidence of such deformation is visible in the microstructure and texture of this specific block of marble. According to Schmid et al. (1987) the lack of visible traces of deformation might be due to an extreme readiness of pure calcite to undergo annealing. An annealing event would at least explain the absence of any intragranular defects and the isotropic grain shapes,

Table 1
Element analysis by ICP-MS on four different samples of the Carrara marble starting material taken from different positions of the Lorano Bianco block (in wt.%)

wt.%	CLB 1A	CLB 1B	CLB 2A	CLB 2B	Average
SiO_2	0.04	0.09	0.08	0.06	0.07
Al_2O_3	0.04	0.07	0.05	0.05	0.05
Fe_2O_3	Trace	0.02	Trace	0.02	0.01
MnO	Trace	Trace	Trace	Trace	Trace
MgO	0.73	0.77	0.99	0.78	0.82
CaO	55.89	54.81	54.63	55.10	55.11
Na_2O	Trace	Trace	Trace	Trace	Trace
K_2O	Trace	Trace	Trace	Trace	Trace
TiO_2	Trace	Trace	Trace	Trace	Trace
P_2O_5	Trace	Trace	Trace	Trace	Trace
Pf	42.80	42.88	42.97	42.65	42.83
Total	99.50	98.64	98.72	98.66	98.88

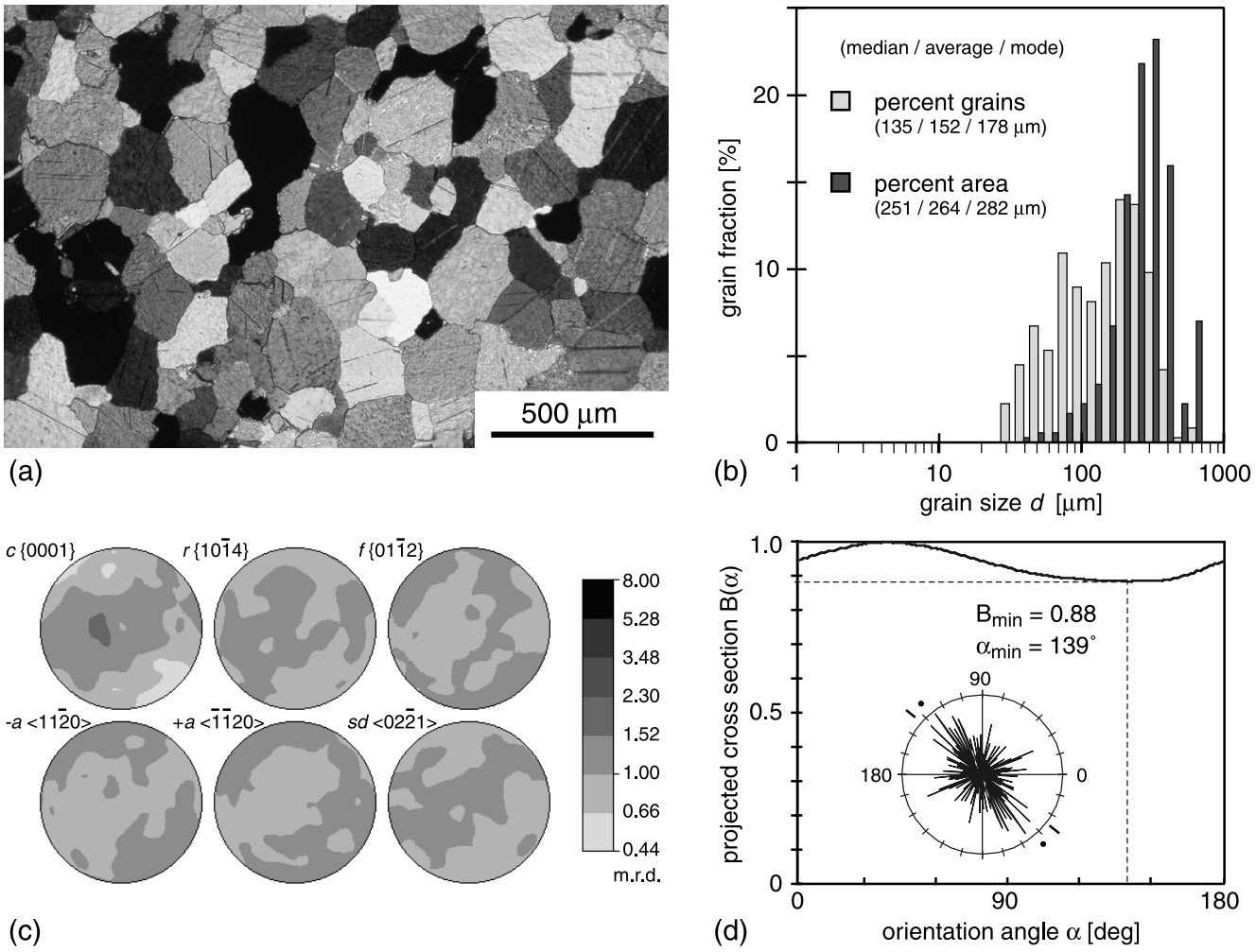

Fig. 2. Microstructure of Carrara marble 'Lorano Bianco' (starting material) with little preferred orientation. (a) *Optical microphotograph* in cross-polarized light. (b) *Grain size distribution* by number and area fractions (in percent) versus grain diameter d (in logarithmic scale). Histograms characterized by median, average and mode. (c) *Fabric diagrams* of crystallographic directions and poles, upper hemisphere equal area projections. (d) *Grain shape analysis*: rose diagram represents the total length of long grain axes per angular interval. Projection diagram displays the total length $B(\alpha)$ of projected grain cross-sections versus orientation angle α, normalized such that at maximum $B(\alpha_{max}) = 1$. The minimum $B(\alpha_{min})$ gives the aspect ratio b/a for an average grain shape ellipse. The smaller B_{min} the stronger is the SPO. Angles α_{min} (tick) and $\alpha_{max} \pm 90°$ (point) indicate the preferred grain shape orientation as marked in the rose diagrams.

but is generally not accepted to erase a preexisting LPO caused by the previous deformation (Rutter et al., 1994). For the purpose of this study, the Lorano Bianco marble block can be considered as an approximately isotropic and homogeneous calcite polycrystal aggregate.

3. Experimental methods

3.1. Deformation apparatus

Deformation experiments were performed in torsion at high temperature and high pressure in an internally heated argon gas medium apparatus (Paterson Instruments Ltd, Canberra), which includes a torsion loading system in addition to the standard axial loading system. The testing column is inserted in a vertically oriented pressure vessel. Externally mounted actuators provide the load and torque that are transmitted to the specimen assembly (Paterson and Olgaard, 2000). The resolution of the axial load and the torque measurements are ± 100 N and ± 1 Nm, respectively. For a typical calcite sample of 15 mm diameter, these loads correspond to a resolution of the normal stress $\Delta\sigma_1$ of ± 0.5 MPa and the shear stress $\Delta\tau$ of ± 1.5 MPa. The temperature gradient across the sample was calibrated to variations smaller than ± 2 K along 30 mm parallel to the column axis. Temperature was measured with a K-type thermocouple placed at about 3 mm from the top of the specimen.

3.2. Sample preparation

Experiments were performed on cylindrical specimens with diameters between 14.7 and 15.0 mm (one with

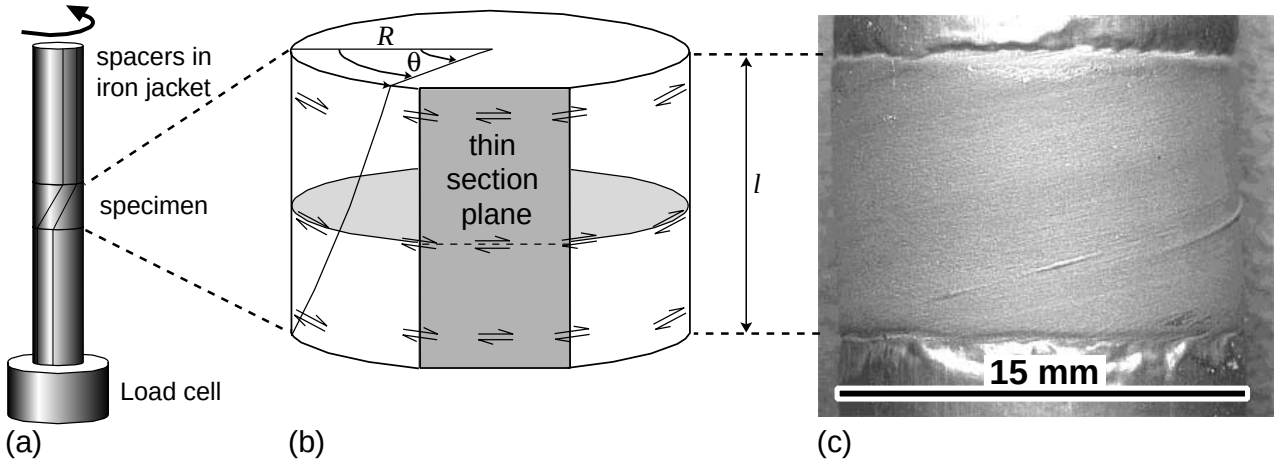

Fig. 3. Setup of the torsion experiment. (a) Torsion column. (b) Schematic drawing of a torsion sample with a section cut typically used for microstructural observations, where R is the radius, l is the length of the cylindrical specimen and θ is the twist angle. (c) Photograph of a deformed sample. The rolling traces on the jacket were initially parallel to the cylinder axis and serve as passive strain markers to illustrate the simple shear deformation in any tangential plane.

9.9 mm) and with a length around 10 mm. The samples were cored perpendicularly to the A side of the block as far as possible from impurities or heterogeneity. The planar cylinder surfaces were machined parallel to each other (within ± 10 μm) and oriented exactly perpendicular to the cylinder axis ($\pm 1°$) by precision polishing. All samples were oven-dried at 100°C for at least 24 h before testing.

3.3. Specimen assembly

The torsion column is shown schematically in Fig. 3a. The cylindrical sample was inserted in a 0.25-mm-thick iron jacket of 15 mm internal diameter, in order to isolate the specimen from the confining argon gas medium. The specimen was sandwiched between alumina (Al_2O_3) spacers of the same diameter. Partially stabilized zirconia (ZrO_2) spacers were inserted between the steel pistons and the alumina spacers in order to optimize the thermal profile. The jacket and the specimen assembly were sealed with O-rings against the steel end pieces at top and bottom.

3.4. Experimental conditions

Two sets of experiments were conducted at temperatures of 1000 ± 2 and 1200 ± 2 K, reaching twist angles between 80 and 840°. The angular displacement rate was kept constant at about 4×10^{-4} rad s^{-1} in each experiment, adjusted for radius and length of the actual samples (see Fig. 3b) in order to obtain a constant shear strain rate of 3×10^{-4} rad s^{-1} at the outer radius, which is equal for all samples. In most runs, deformation was homogeneous on the outer surface of the specimen, as indicated by the almost constant inclination of initially vertical strain markers on the jacket after the experiment (Fig. 3c).

At 1200 K it was not possible to perform experiments to γ larger than five in a single run because the jackets always failed. Although various explanations were put forward (α–Fe $\rightarrow$ γ–Fe transition of the jacket at 1185 K at room pressure; reaction embrittlement) and tested (run at 1165 K in the α–Fe stability field; isolation with thin platinum foil), none were satisfactory to identify the problem. A higher shear strain was finally reached by interrupting the experiment at intermediate strain, re-jacketing the specimen and returning to experimental conditions to continue the run. Because the jacket strength (about 0.5% of the total torque) was below the experimental reproducibility, no correction was applied for it.

3.5. Strain distribution

In order to evaluate the strain distribution in the specimen during torsion testing, a split cylinder specimen of Carrara marble was prepared and a gold foil was inserted between the two halves (Fig. 4a). The sample was twisted approximately 360° at 1200 K, corresponding to a shear strain of $\gamma = 2.5$ at a strain rate of 3×10^{-4} s^{-1} at the outer radius. The sample deformed perfectly homogeneous without any visible strain localization. The specimen was sliced perpendicular to the cylindrical axis every 2 mm to check how the gold foil orientation changed from the bottom to the top of the sample (Fig. 4b). In all such cuts, the intersection of the

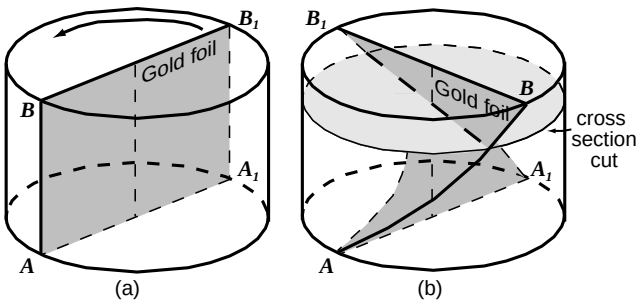

Fig. 4. Sketch of a split specimen: (a) before deformation, and (b) after deformation. The intersection of the gold foil with any plane normal to the cylinder axis is a straight line passing through the cylinder axis.

gold foil with the circular cylinder plane was a straight line at increasing azimuth angle with respect to a reference marker and this angle was proportional to the distance from the bottom spacer. Inside the cylinder, the gold foil therefore developed a helicoidal shape after the deformation, confirming that shear strain and strain rate increase proportionally to the radius, and are homogeneous along the cylinder.

3.6. Rheological analysis of the torsion test

The theory on the deformation of a uniform (right circular) cylinder under torsion load is based on the assumption that strain is homogeneous along the cylinder length and constitutes locally simple shear (e.g. Handin et al., 1960; Paterson and Olgaard, 2000). The relation of angular displacement θ (in radians) between the ends of a cylinder of length l to local shear strain γ_r at any radius r is (see Fig. 3b):

$$\gamma_r = \frac{r}{l}\theta \tag{1}$$

and analogously for their respective rates it is:

$$\dot{\gamma}_r = \frac{\mathrm{d}\gamma_r}{\mathrm{d}t} = \frac{r}{l}\dot{\theta}. \tag{2}$$

The radius is $r = R$ at the outer sample surface. It is a reasonable assumption for most relevant materials, that the solid cylinder deforms under a power law rheology $\dot{\gamma}_r \propto \tau_r^n$ with constant parameters anywhere in the sample. Then the shear stress at any radius r is:

$$\tau_r = \left(\frac{r}{R}\right)^{1/n}\tau_R \tag{3}$$

and the shear stress at maximum radius $r = R$ relates to the torque M applied to the cylinder by:

$$\tau_R = \frac{3 + 1/n}{2\pi R^3}M. \tag{4}$$

The stress exponent n can be determined from twist rate stepping tests as the slope of the line in a log–log diagram of $\dot{\theta}$ versus M according to:

$$\log\dot{\theta} = n\log M + \text{const.} \tag{5}$$

Further, the torque ratio applied to two samples with different radii to be twisted at the same nominal angular displacement rate $\dot{\theta}/l$ is:

$$\frac{M_1}{M_2} = \left(\frac{R_1}{R_2}\right)^{3+1/n} \tag{6}$$

as displayed in Fig. 5a. For deformation with a high stress exponent n, the applied torque is rather insensitive to reasonable changes in n. A sample of half the radius requires a torque about eight times less to deform at the same twist rate. This shows that most of the torque is supported by the outer rim of the torsion cylinder. The applied shear stress within the sample increases non-linearly with radius according to Eq. (3) and is quite sensitive to the actual value of n (Fig. 5b). For high exponents ($n \geq 10$), the shear stress remains nearly constant for $r > R/2$. This implies that for microstructural observations the stress-sensitive grain size distributions can be measured on planar tangential section cuts, as long as those are cut less than half the sample radius away from the outer surface.

3.7. Microstructural studies in torsion specimens

Microstructural studies of specimens from torsion tests are complex compared with conventional axial deformation tests because of the strain gradient along the radius. The specimen can be cut in three principal ways (Paterson and Olgaard, 2000):

(a) *Cut perpendicular to the cylinder axis.* The section plane contains the shear displacement. Shear strain, strain rate and shear stress increase with radius across the section from zero at the cylinder center to their maximum at the edge.
(b) *Cut parallel to the cylinder axis through the cylinder center.* The shear direction is normal to the section. Shear

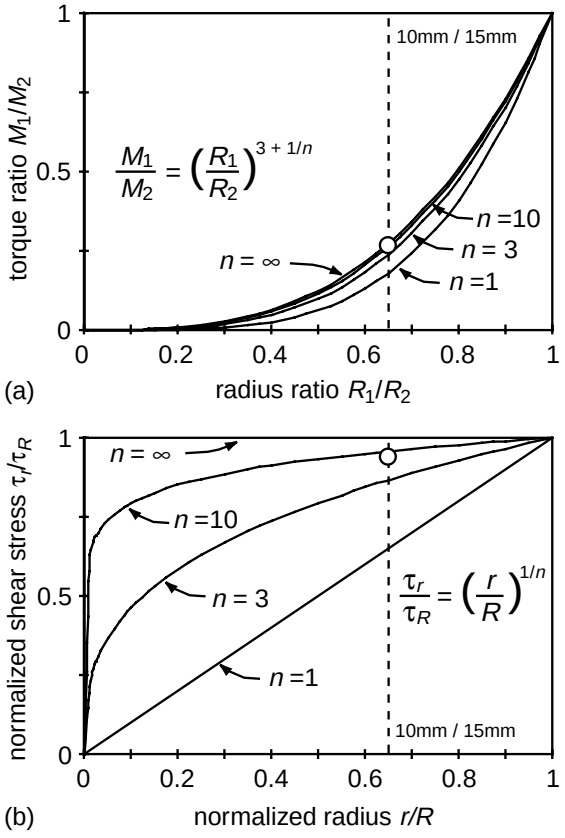

Fig. 5. Theoretical torque and stress distributions versus cylinder radius, assuming a homogeneous flow law and various stress exponents n. (a) Torque ratio versus radius ratio of two samples with different radii. (b) Shear stress versus normalized radius within a sample. The radius ratio (dashed lines) and the experimental torque and stress ratios (open circles) between 10 and 15 mm diameter specimens are indicated.

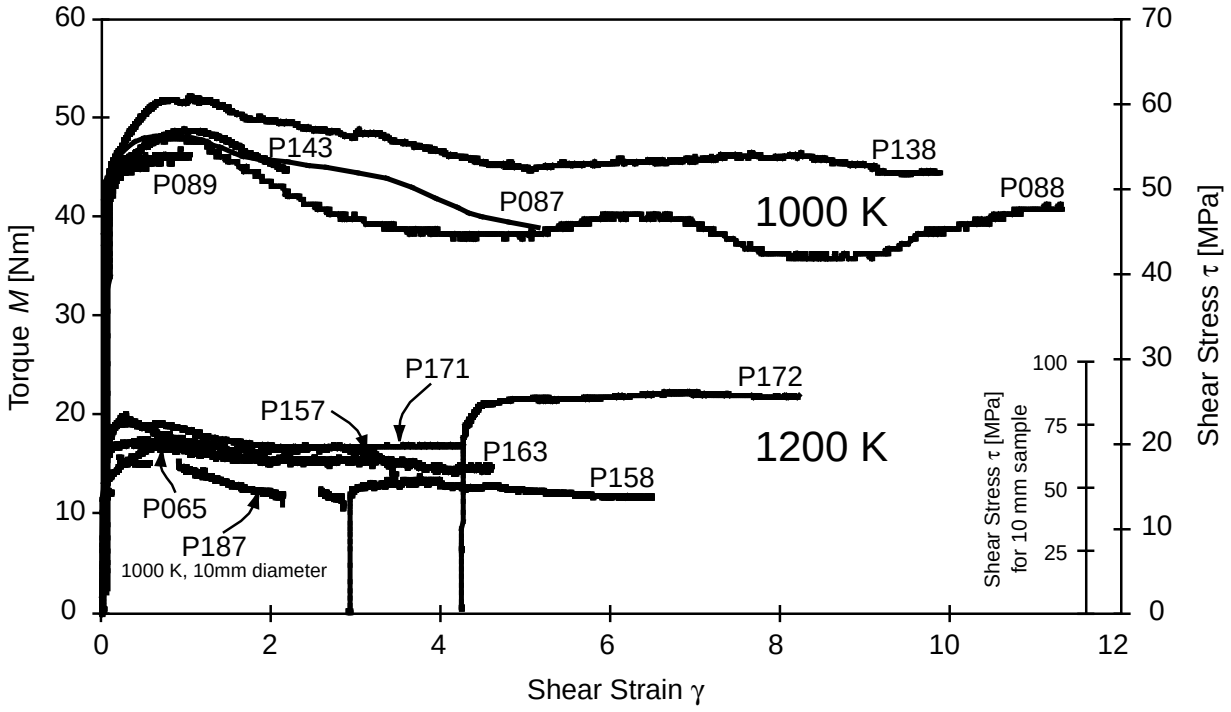

Fig. 6. Torque versus shear strain for all constant strain rate tests at 1000 and 1200 K (for run characteristics see Table 2). The torque is converted into shear stress on the scale to the right after Eq. (4) assuming 15 mm (inset 10 mm) diameter samples and a stress exponent $n = 10$.

strain, strain rate and shear stress increase with radius across the section from zero at the cylinder center to their maximum at the edge.

(c) *Cut parallel to the cylinder axis close to the outer surface.* The shear direction is approximately parallel to the section. Shear strain, strain rate and shear stress are nearly constant across such sections. Their variations increase with section width (Pieri et al., 2001).

We chose mode (c) to cut our deformed specimens for microstructural examinations, as shown in Fig. 3b. In this way, microstructural information is given in the standard reference frame typically used for observations of naturally deformed mylonites, with the section cut normal to the foliation containing the lineation. All thin sections were prepared ultra thin (<10 μm) and polished on both sides.

3.8. Microstructural quantification

Analyses of grain size and shape were performed on tracings of grain boundaries manually digitized from optical photographs. Grain sizes, d, were calculated from the measured areas assuming d as the diameter of a circle with the same area. Grain size histograms were plotted both as frequency and area fractions versus log (d) in order to visualize the bimodal distributions in some of the samples.

The software packages IMED'OULINE, SCASMO and PAROR (Panozzo, 1983, 1984) were employed to calculate the area weighted SPO of grains. Data are presented in rose diagrams, which show the angular distribution of grain long axes, and in projection diagrams, which give the orientation and aspect ratio of an average grain shape ellipse. Markers indicate the orientation of the measured shape ellipse and of the theoretical strain ellipse[2] for the imposed shear strain γ in the rose diagrams.

3.9. Method for LPO measurements

Texture measurements were performed by electron backscatter diffraction (EBSD) using a scanning electron microscope (CamScan CS44LB). The EBSD patterns were indexed using software OIM version 2.0 (TSL Inc.). The system automatically collects large amounts of orientation data and provides spatially resolved orientation mapping on predefined grids by either beam or stage scans (Adams et al., 1993). Data sets of individual orientations were processed by Gaussian convolution with half width of 15° and maximum expansion $L = 22$ within the harmonic calculus. Fabric diagrams of specific crystallographic poles and directions were derived and plotted using software BEARTEX (Wenk et al., 1998). Applications of EBSD to deformed rocks have recently been reviewed by Prior et al. (1999) and Leiss et al. (2000).

[2] The strain ellipse has theoretically an aspect ratio $b/a = 2/(\gamma^2 + 2 + \gamma\sqrt{\gamma^2 + 4})$ and an orientation angle $\alpha = \arctan(2/\gamma)/2$ as a function of shear strain γ (Ramsay and Huber, 1983).

4. Results on rheology

4.1. Torque and stress versus strain

In this study, strain rate and temperatures were chosen to reproduce previously explored experimental conditions (Schmid et al., 1987), and to expand those tests to shear strains, that are an order of magnitude higher. At the experimental temperatures of 1000 and 1200 K and at the shear strain rate of $3 \times 10^{-4}\,s^{-1}$, the marble is expected to deform within the dislocation creep regime (Regime 2 of Schmid et al. (1980) with power law exponent $n = 7.6$). The test series at either temperature should theoretically differ only by various amounts of shear strain γ (Fig. 6 and Table 2). At 1000 K, a peak torque of 48 ± 4 Nm was reached at $\gamma \approx 1$, followed by 10% strain weakening. A steady-state torque of 44 ± 4 Nm was established for $\gamma > 5$. At 1200 K, a peak torque of 18 ± 2 Nm was reached at $\gamma \approx 0.5$, followed by 6% strain weakening, and a steady-state torque of 17 ± 2 Nm was reached at $\gamma > 2$. This behavior is similar to the runs at 1000 K, but happens at comparably lower torque and shear strain. Re-jacketing the samples resulted in a torque larger (run P172) or smaller (run P158) than that of the sample variability (runs P065, P157, P163 and P171) and reduced the experimental reproducibility. The variations among individual runs at the same experimental conditions are primarily due to small differences in specimen diameters (a difference of 0.3 mm in diameter corresponds to 6% variation in torque). The torque scale was converted into shear stress at the outer cylinder radius (Fig. 6 at right) using Eq. (4) with a constant stress exponent $n = 10$ and a cylinder diameter of 15 and 10 mm, respectively, such that the shear strength can be compared with previous experimental work.

4.2. Power law stress exponent

Stepping strain rate tests (Fig. 7a) were performed in order to determine the value of the stress exponent n at various shear strains in the following way:

(a) The specimen was twisted as usual at a defined angular displacement rate corresponding to a shear strain rate of $3 \times 10^{-4}\,s^{-1}$ at the outer cylinder surface until the shear strain of interest was reached.
(b) The twist rate was decreased approximately by an order of magnitude and kept constant until the torque reached a new equilibrium value (only on experiments at 1000 K; at 1200 K it was not possible to decrease the strain rate because the corresponding torque variations were below the resolution of the torque cell).
(c) The twist rate was stepwise increased in several small increments even above the initial rate, covering in total about 2.5 orders of magnitude.
(d) The twist rate and corresponding torque values were plotted in a log–log-diagram (Fig. 7b). The stress exponent n is determined as the slope of the linear fit of the data according to Eq. (5).

At 1000 K, the stress exponent n decreased monotonously from 10.0 ($\gamma = 1.2$) to 5.8 ($\gamma = 9$). At 1200 K, the exponent n was only evaluated up to $\gamma = 5$, and its value remained between 10.4 and 12.6. As the accessible strain rate interval at 1200 K was narrow because the torque resolution was limited, the n exponent could only be roughly estimated.

Table 2
Experimental conditions and specimen dimensions for the performed runs. All samples were deformed at a shear strain rate of $(3.0 \pm 0.1) \times 10^{-4}\,s^{-1}$ at the outer cylinder radius, except during the stepping tests. The specimen with 10 mm diameter (run P187) was deformed at an equivalent twist rate such that the shear strain rate at any radius was the same as in the 15 mm samples

Run #	Temperature (K)	Sample #	Diameter $2R$ (mm)	Length l (mm)	Total twist θ (rad)	Shear strain γ	Remarks
P087	1000	CLB 1-8	14.98	10.41	7.0	5.0	
P088	1000	CLB 1-9	14.95	10.46	15.9	11.4	
P089	1000	CLB 1-10	14.94	10.46	1.4	1.0	
P138	1000	CLB 2-7	14.71	8.80	12.1	10.1	
P143	1000	CLB 2-8	14.98	9.50	3.0	2.3	
P148	1000	CLB 2-11	14.89	10.70	15.4	10.7	Stepping
P187	1000	CLB 2-19	9.87	9.34	5.4	2.9	Stepping, 10 mm diameter
P065	1200	CLB 1-4	14.96	20.29	2.4	0.9	
P154	1200	CLB 2-13	14.89	10.79	8.3	5.7	Stepping
P157	1200	CLB 2-14	14.82	10.30	4.8	3.5	Only top part of cylinder[a]
P158	1200	CLB 2-15	14.81	7.00	3.4	7.0	P157 continued after re-jacketing
P163	1200	CLB 2-16	14.75	9.80	5.9	4.4	
P171	1200	CLB 2-17	14.78	9.40	5.4	4.3	
P172	1200	CLB 2-18	14.78	9.26	5.0	8.2	P171 continued after re-jacketing

[a] Deformation localized in the bottom part of the specimen. The sample was cut perpendicular to the cylinder axis. The shear strain was estimated for the homogeneously deformed top part using the inclined rolling traces on the iron jacket.

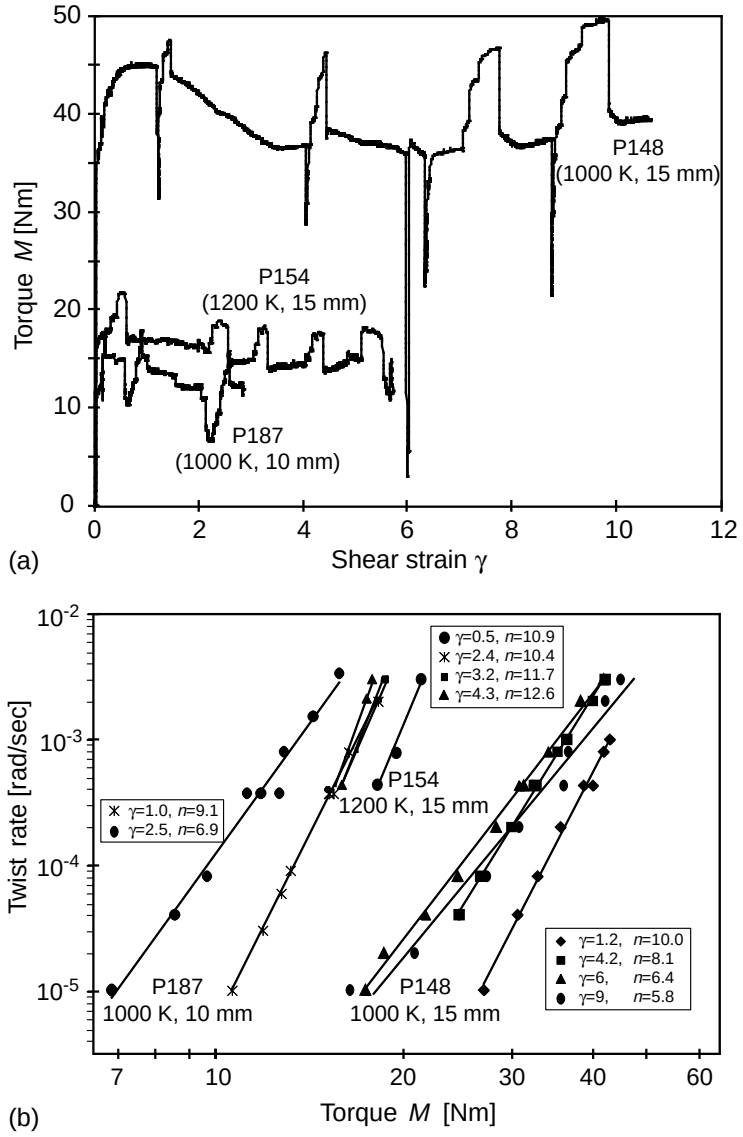

Fig. 7. Strain rate stepping tests at 1000 K on 10 and 15 mm diameter specimens, and at 1200 K on 15 mm diameter specimen. (a) Torque versus shear strain. (b) Twist rate versus torque in a log–log plot. The slopes of the fitted lines give the stress exponent n for the respective temperature and shear strain. Note that the slopes are very similar for the 10 and 15 mm diameter samples at 1000 K.

4.3. Radial stress distribution

The validity of the applied conversion from torque to shear stress according to Eq. (4) was tested by comparing the torque on specimens with 10 and 15 mm diameters deformed at the same twist rate. The torque for the 10-mm-diameter sample was nearly four times smaller than that for the 15-mm-diameter samples (Fig. 6), but the calculated shear stresses at the outer radius for the two sample sizes were similar (Fig. 6, scale at right). This implies that the shear stress is nearly constant in a wide portion of the solid cylinder, in agreement with Eq. (3) and Fig. 5b. Also, the stress exponent n for the 10-mm-diameter sample showed a trend very similar to that obtained for the 15-mm-diameter sample, as decreasing from 9.1 ($\gamma = 1$) to 6.9 ($\gamma = 2.5$). This verified the applied assumption that the rheology was constant in the larger portion of the cylindrical specimen, at least between 10 and 15 mm diameter.

5. Microstructural analysis

5.1. Microstructural evolution at 1000 K

5.1.1. Shear deformation microstructure

The microstructure after a shear $\gamma = 1$ (sample P089) is characterized by large elongate stretched grains with a grain size similar to that of the starting material, and by subgrains and few small new grains along the grain boundaries (Fig. 8a). Optical strain features like undulose extinction and deformation bands are common. Thick twins, which are lensoidal shaped and bent, indicate intracrystalline

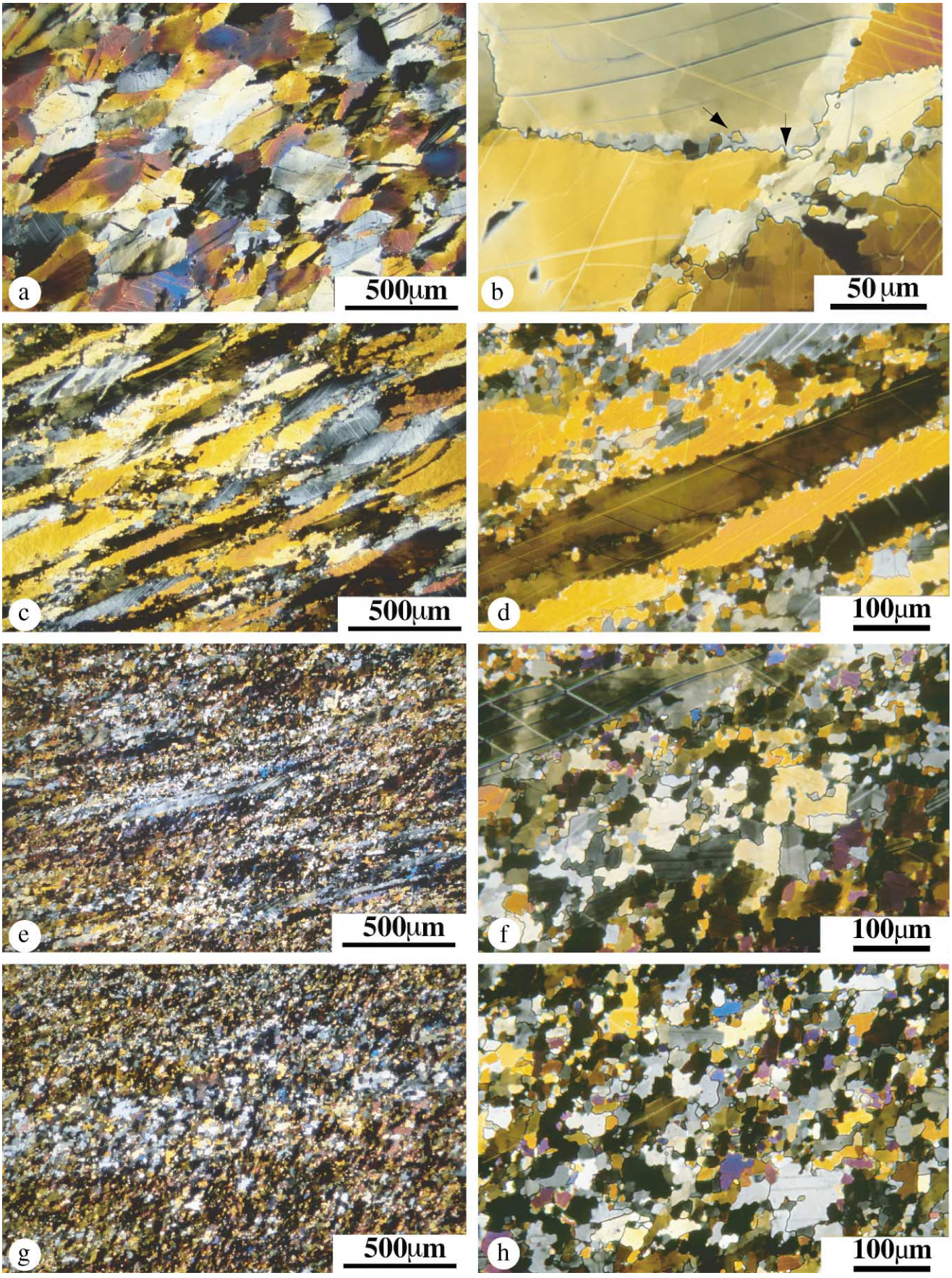
a
500μm
b
50 μm
c
500μm
d
100μm
e
500μm
f
100μm
g
500μm
h
100μm

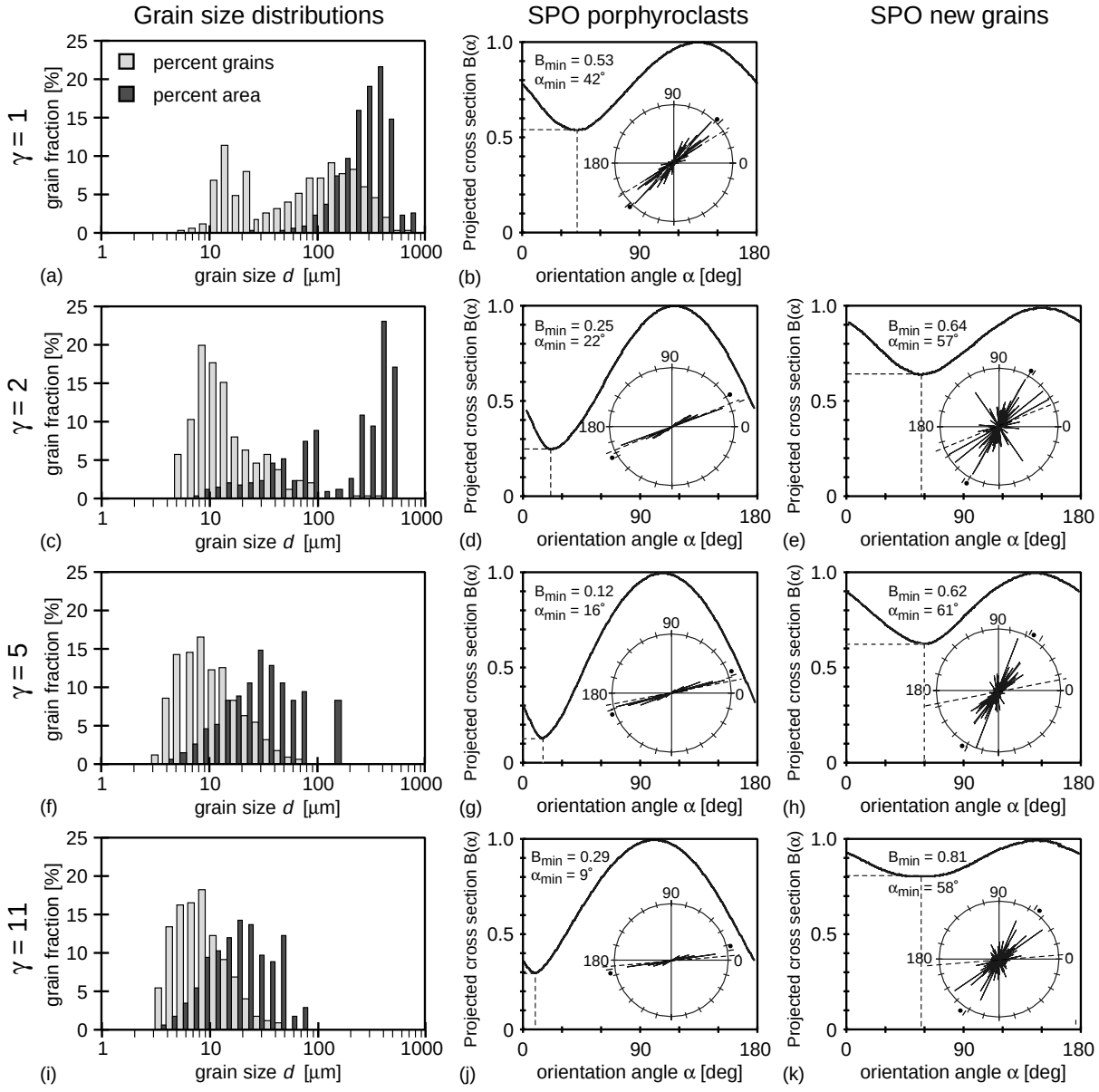

Fig. 9. Grain size distribution and grain shape analysis of samples deformed at 1000 K to $\gamma = 1$ (a, b), $\gamma = 2$ (c–e), $\gamma = 5$ (f–h), $\gamma = 11$ (i–k). For explanations see Fig. 2. Orientation of the theoretical finite strain ellipse marked in the rose diagrams (dashed line).

deformation along with twin boundary migration. The thin and straight twins present in many grains were probably introduced during depressurization and cooling at the end of the experiment. Grain boundaries are sutured and serrated. Bulges have a wavelength of approximately 10 μm. Recrystallization occurred mainly by bulge nucleation and in some cases by subgrain rotation (Fig. 8b). The grain size histogram in number fractions shows a well defined bimodal distribution, which is not as evident with area fractions (Fig. 9a) because the recrystallized grains with an average grain size of 10 μm make up only 1–2% of the sample. The porphyroclasts show a marked SPO (Fig. 9b) with aspect ratio of 0.5 and preferred orientation angle at 42° with respect to the shear zone boundary (SZB). Because the SPO was determined on micrographs from a section cut somewhat inside the sample, the measured values for both aspect ratio and orientation angle correspond to a lower shear strain than $\gamma = 1$.

Fig. 8. Microphotographs in cross-polarized light of samples deformed in torsion at 1000 K to shear strain of $\gamma = 1$ (a, b), $\gamma = 2$ (c, d), $\gamma = 5$ (e, f) and $\gamma = 11$ (g, h). Overviews at low magnification (at left) and details at higher magnifications (at right). Shear zone boundary is oriented parallel to the long edge of the image and the sense of shear is dextral. The arrows in (b) point to a small leftover grain and to bulging of the grain boundary, indicating that the horizontal grain boundary is migrating downwards.

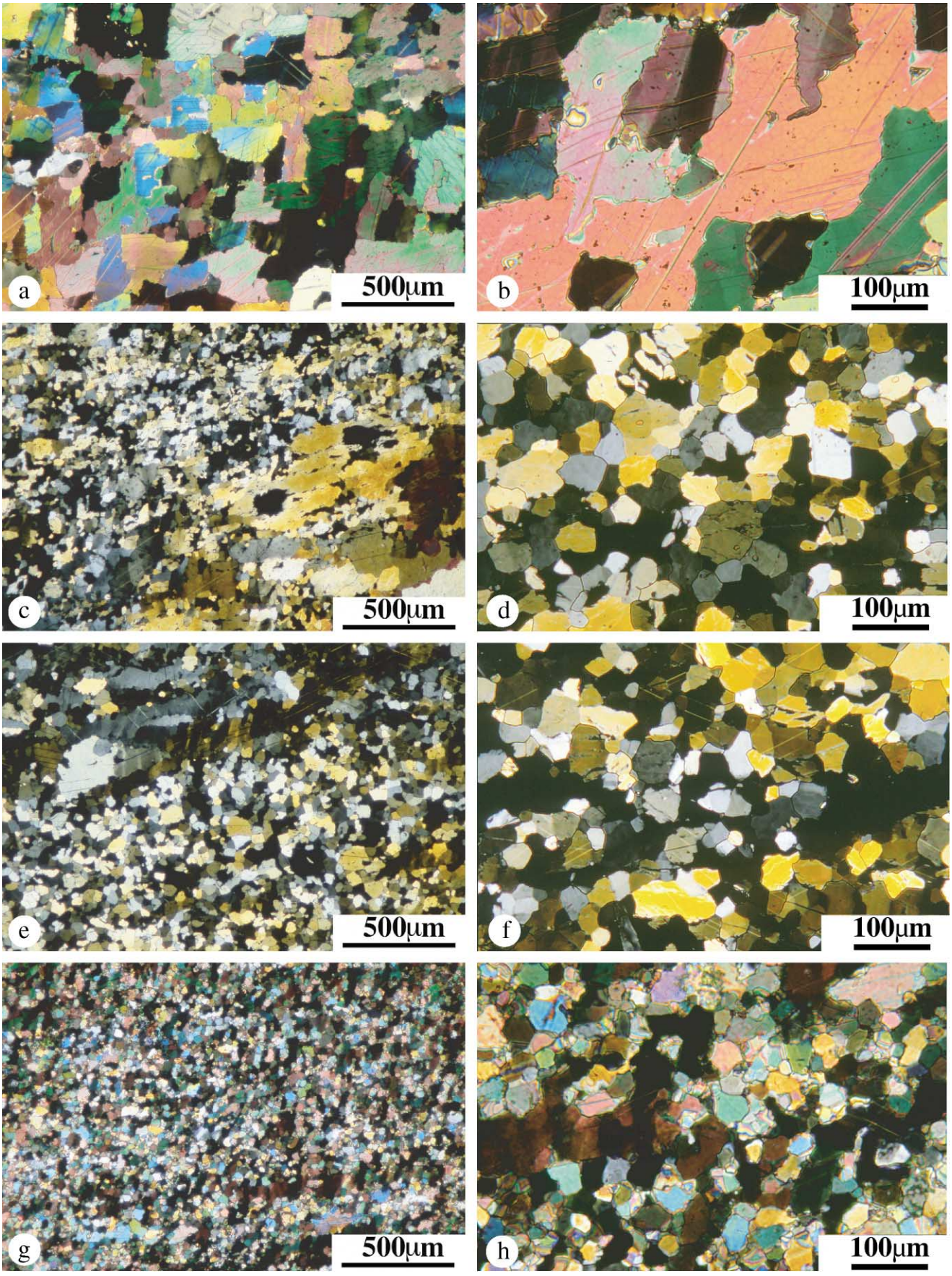
a
500μm
b
100μm
c
500μm
d
100μm
e
500μm
f
100μm
g
500μm
h
100μm

5.1.2. Transient core-and-mantle microstructure

In the microstructure after deformation of $\gamma = 2$, stretched porphyroclasts show indications for intracrystalline deformation (Fig. 8c and d). They define a foliation oblique to the SZB and track the finite amount of imposed bulk shear. The porphyroclasts represent only 2–3% of the total number of grains, but occupy over 80% of the area (Fig. 9c). They are often surrounded by a fine grained recrystallized matrix making up 18% of the sample. The dynamically recrystallized grain size is 10 μm on average. The newly formed grains have a high aspect ratio and a steep preferred orientation to the SZB (Fig. 9e), which are both not representative for the imposed bulk shear. The porphyroclasts show a marked aspect ratio of 0.25 and are rotated towards the SZB at an angle of 22°, resembling very closely the theoretical values for the finite strain ellipse (Fig. 9d).

5.1.3. Recrystallization microstructure

At strain $\gamma = 5$, the original microstructure is strongly overprinted by dynamic recrystallization. The remaining coarse grains are extremely elongate and strongly oriented in a foliation at a small angle to the SZB. They have very irregular and sutured boundaries and are dispersed in a fine grained matrix which makes up 80% of the area (Fig. 8e and f). The fine matrix consists of equant small grains with an average size of 10 μm, as shown in the number fraction histogram, and of larger grains (30–40 μm), which are well represented in the area fraction histogram (Fig. 9f). The small grains display an oblique SPO in an angle of about 60° to the SZB, while the relic grains have rotated further towards the SZB and show an extremely pronounced aspect ratio (Fig. 9g and h).

In the highest strained sample ($\gamma = 11$), dynamically recrystallized grains make up more than 95% of the specimen (Fig. 8g and h). The few porphyroclasts have slightly smaller sizes than observed for lower strain. The grain size distribution (Fig. 9i) is bimodal with peaks between 5 and 15 μm (in number fractions) and around 20–50 μm (in area fractions), similarly to the sample deformed to $\gamma = 5$. The aspect ratio of the porphyroclasts is less pronounced than that in the specimen deformed to $\gamma = 5$ (Fig. 9j), and deviates significantly from the value expected for the strain ellipse at this strain level. Since most porphyroclasts have not only been sheared but partially consumed by recrystallization, they have reduced their dimensions and rounded their shapes. The newly formed grains show a weak SPO, which is primarily due to a preferred alignment of grain boundaries at a large angle to the SZB, defining a steep secondary foliation, S_2, at about 60° to the SZB (Fig. 9k).

5.2. Microstructural development at 1200 K

5.2.1. Grain boundary migration microstructure

The grain shape after deformation to $\gamma = 1$ at 1200 K is profoundly different to that at similar strain at 1000 K due to extensive grain boundary migration. Many grain boundaries were preferentially oriented parallel and at 70–75° to the shear direction (Fig. 10a and b). This kind of microstructure has already been observed in simple shear tests on calcite at similar temperatures (Schmid et al., 1987). Some grains have grown considerably at the expense of others, although the average grain size is somewhat reduced (Fig. 11a). The migrated grain boundaries are curved and sometimes sutured. Undulose extinction and deformation bands are common, and subgrains are visible. New grains start to develop along the grain boundaries. The SPO is weak (Fig. 11b), and the shape of the porphyroclasts is mainly determined by grain boundary migration rather than by the shear deformation. It would not be possible to infer the sense of shear if the SZB had not been known.

5.2.2. Recrystallization microstructure

The microstructure for shear strain of $\gamma = 4.5$ is characterized by coarse porphyroclasts with irregular and lobate boundaries. Patches of recrystallized small equant grains (around 35 μm) cover about 25–30% of the total area but contain the majority of grains (Fig. 10c and d), which results in a bimodal grain size distribution (Fig. 11c). The newly formed grains display a weak aspect ratio with the majority of long axes oriented between 30 and 70° with respect to the SZB (Fig. 11d).

For a shear strain of $\gamma = 6.5$, about 30% of the microstructure is composed of newly formed grains (around 45 μm) that are almost equant in shape and have straight boundaries (Fig. 10e and f). Large stretched porphyroclasts (grain size up to 250 μm), which show incipient recrystallization by subgrain rotation, still cover more than half the area (Fig. 11e). The recrystallized grains have a weak aspect ratio and their long axes are steeply oriented with respect to the SZB (Fig. 11f).

At a shear strain of $\gamma = 8.5$, the microstructure has almost completely recrystallized to a homogeneous matrix of fine grains of about 20 μm (Fig. 10g and h). The few porphyroclasts still present are strongly elongated and rich in twins. The grain size distribution is unimodal, visible in the overlapping area fraction and percent grain histograms (Fig. 11g). The newly formed grains show a SPO with weak aspect ratio oriented at about 60° with respect to the SZB (Fig. 11h), which is mostly due to a preferred alignment of grain boundaries.

Fig. 10. Microphotographs in cross-polarized light of samples deformed in torsion at 1200 K to shear strain of $\gamma = 1$ (a, b), $\gamma = 4.5$ (c, d), $\gamma = 6.5$ (e, f) and $\gamma = 8.5$ (g, h). Overviews at low magnification (at left) and details at higher magnifications (at right). Shear zone boundary is oriented parallel to the long edge of the image and the sense of shear is dextral.

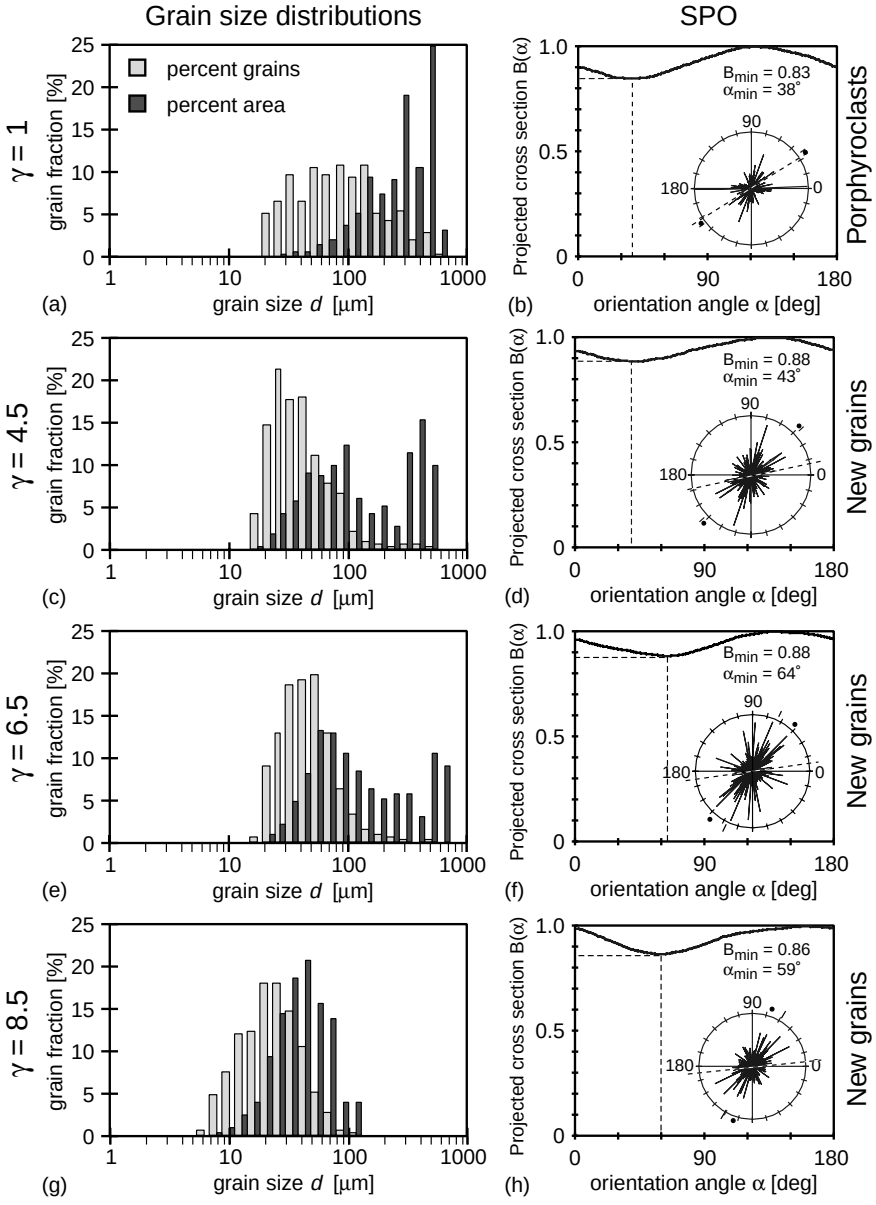

Fig. 11. Grain size distribution and grain shape analysis of samples deformed at 1200 K to $\gamma = 1$ (a, b), $\gamma = 4.5$ (c, d), $\gamma = 6.5$ (e, f), $\gamma = 8.5$ (g, h). For explanations see Fig. 2. Orientation of the theoretical finite strain ellipse marked in the rose diagrams (dashed line).

5.3. Lattice-preferred orientation

The LPO evolution with shear strain is illustrated in fabric diagrams of the main crystallographic directions and poles (Fig. 12). For low strain, typical deformation textures of moderate strength developed with monoclinic sample symmetry and an oblique *c*-axis distribution at both temperatures. The texture at 1000 K consists of several orientation components with $c\{0001\}$ and $r\{10\bar{1}4\}$ planes in the shear plane and with $a\langle\bar{1}2\bar{1}0\rangle$ and *s.d.*$\langle02\bar{2}1\rangle$ directions parallel to the shear directions (Pieri et al., 2001). At 1200 K, the main component has the $c\{0001\}$ plane in the shear plane and $a\langle\bar{1}2\bar{1}0\rangle$ directions parallel to the shear direction. The latter texture was observed under similar conditions by Schmid et al. (1987) and characterized as grain boundary migration texture. The LPO evolution with further strain during dynamic recrystallization shows remarkable differences at 1000 and 1200 K, though a similar pattern is ultimately reached at high shear strain ($\gamma > 8$) for both temperatures, which consists of an extremely strong texture with a main texture component $r\{10\bar{1}4\}$ $a\langle\bar{1}2\bar{1}0\rangle$ and a minor component $c\{0001\}$ $a\langle\bar{1}2\bar{1}0\rangle$.

Six ideal orientations of particular interest in the LPO evolution (Pieri et al., 2001) are highlighted in orientation maps shown for the samples deformed to maximum γ at both temperatures (Fig. 13). These orientations consist of two conjugate pairs of ideal orientations D1/D2 and C1/C2, which transfer into each other by a 180° rotation about the section normal, and of the orientations A and B, which transfer into each other by a 180° rotation about the shear

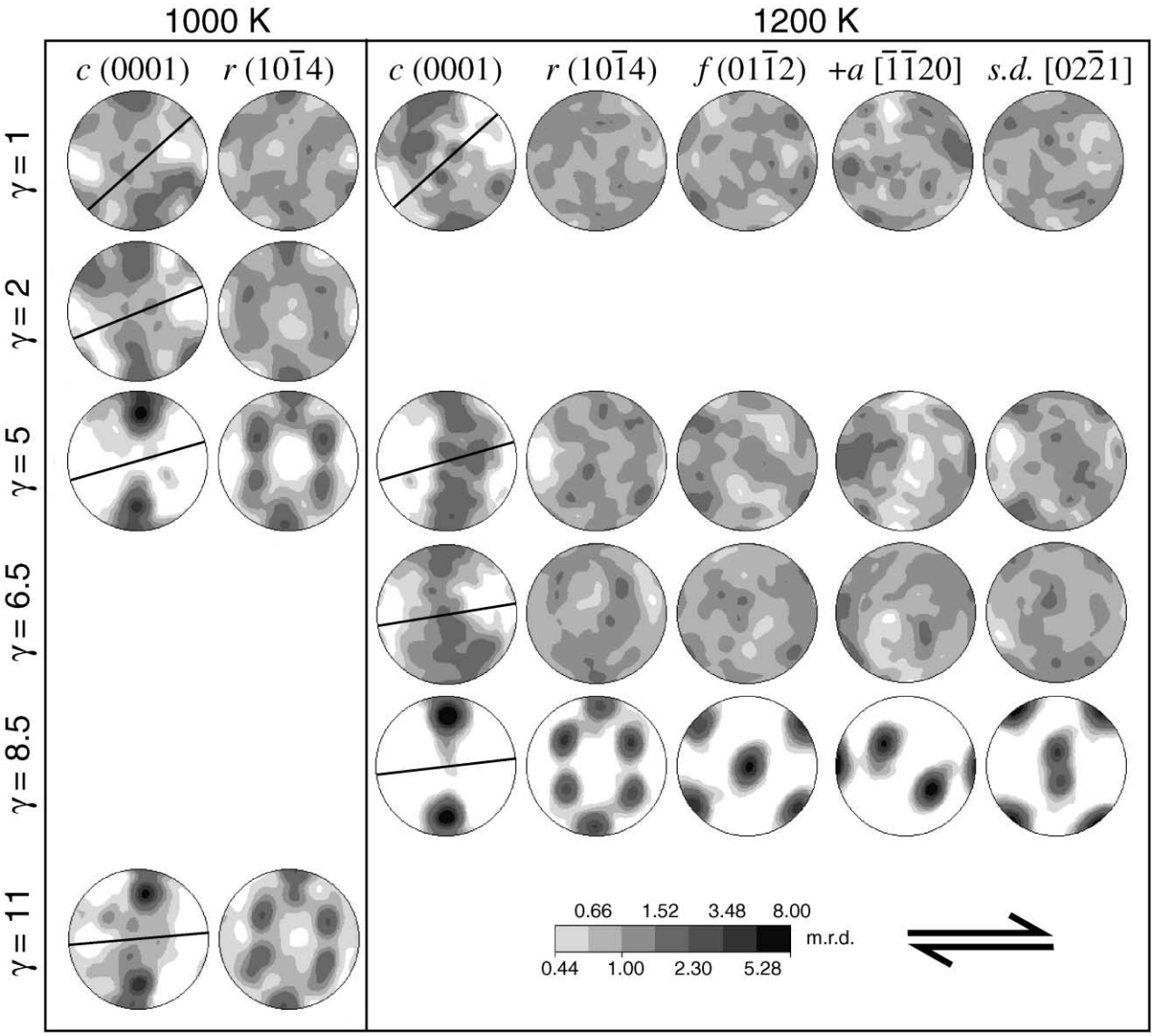

Fig. 12. Fabric diagrams of crystallographic directions and poles of Carrara marble deformed in torsion. Orientation densities in multiples of random distribution (m.r.d.) in logarithmic scale, upper hemisphere equal area projections. The orientation of the theoretical strain ellipse is indicated by a line in the *c*-axis diagrams.

direction. The orientations A, B and D1/D2 characterize the LPO at low strain (*deformation texture*, $\gamma \leq 2$). The orientations C1/C2 develop at high strain (*recrystallization texture*), where A and B contribute negligibly to the texture. At high strain, more than 50% of the total sample area has crystal orientations in the $r\{10\bar{1}4\}\, a\langle\bar{1}2\bar{1}0\rangle$ component (C1/C2 orientations) and in the $c\{0001\}\, a\langle\bar{1}2\bar{1}0\rangle$ component (D1/D2 orientations), both defined with 25° tolerance. This recrystallization texture did not change significantly between $\gamma = 5$ and $\gamma = 11$ at 1000 K, but was not observed before $\gamma = 8$ at 1200 K.

6. Discussion

Carrara marble undergoes profound changes in rheology, microstructure and texture as it deforms within the dislocation creep (power law) regime to high shear strain. Moderate strain weakening (≤10%) was observed at both experimental temperatures followed by mechanical steady-state. High shear strain is required before steady-state establishes for the recrystallization microstructure and texture.

6.1. Mechanical steady-state

In previous work on Carrara marble (Schmid et al., 1980), a steady-state flow stress was thought to have been achieved after a few percent compression (10–15% strain, equivalent to $0.17 \leq \gamma \leq 0.25$). Strain weakening, however, was observed at larger strain by Schmid et al. (1987) in simple shear experiments. Our results indicate that Carrara marble undergoes strain hardening until a peak stress is achieved at

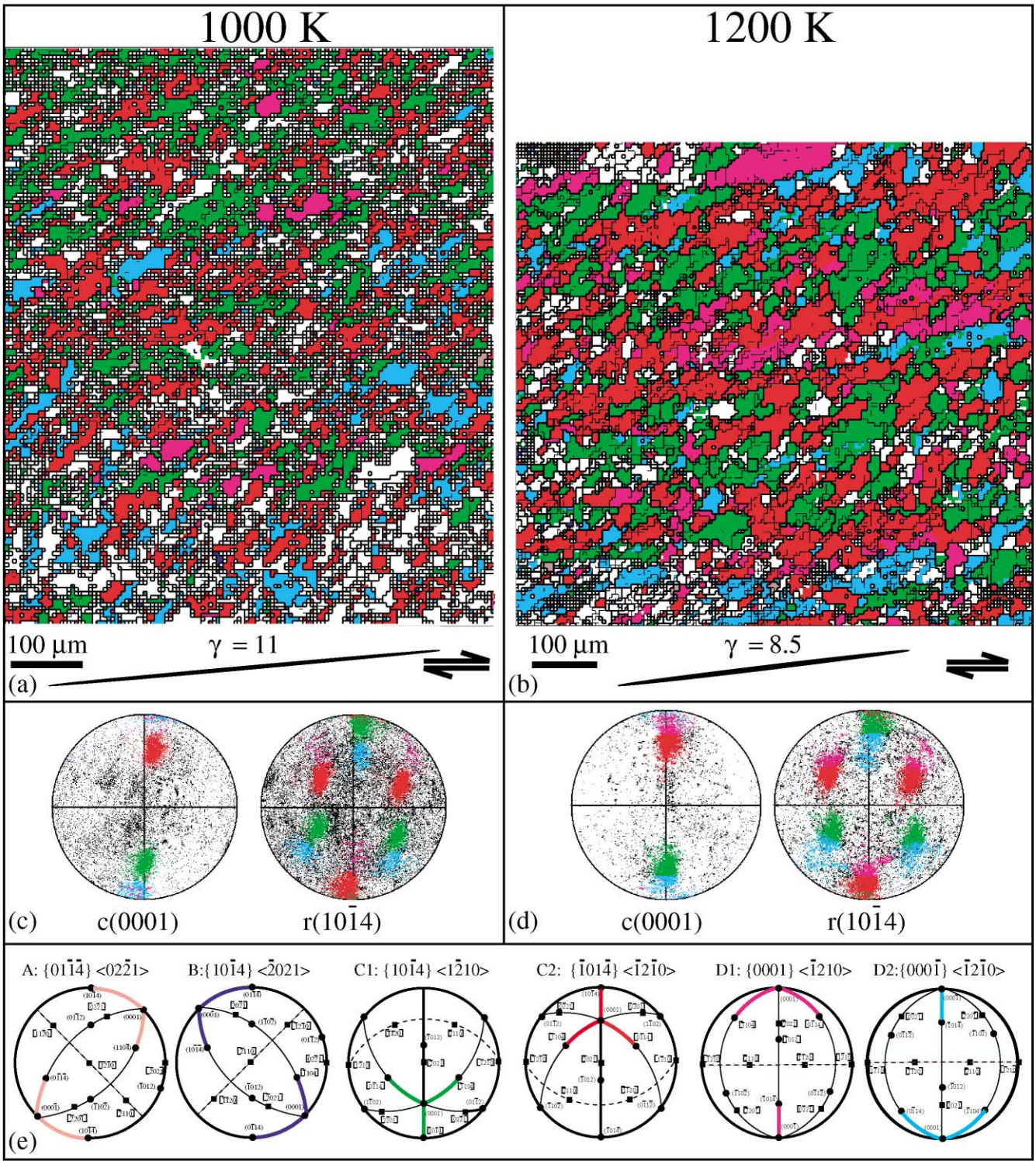

Fig. 13. Spatial orientation analysis for the high strain tests at 1000 K ($\gamma = 11$, left column) and 1200 K ($\gamma = 8.5$, right column). (a, b) *Orientation imaging maps*. Crystal orientations are highlighted according to color key for six texture components given below. Nearest neighbor misorientations marked by thin (subgrain boundaries) or thick lines (grain boundaries) for misorientation angles between 5 and 15° and larger than 15°, respectively. Theoretical strain ellipses indicated, dextral sense of shear. (c, d) *Pole figures* of the raw data with the specified orientations highlighted. (e) *Stereograms* of six ideal orientations as defined by Pieri et al. (2001). Components A, B, D1 and D2 characterize the deformation texture. C1 and C2 characterize the recrystallization texture and dominate here.

$\gamma \leq 1$ (45% strain), followed by strain softening. Therefore, many of the previous strength measurements made with compression tests may not have reached mechanical steady-state.

6.2. Deformation mechanisms

The experimental conditions of this study were plotted in a deformation mechanism map of shear stress versus grain size at constant shear strain rate (Fig. 14). The shear stress at the starting conditions is in good agreement with the deformation mechanism map. As predicted, the starting material deformed within the power law regime with high n at shear stress of 60 ± 5 MPa at 1000 K and of 20 ± 3 MPa at 1200 K.

While the starting grain size plots in the grain size insensitive (power law) field, the measured recrystallized grain sizes fall into the grain size sensitive field with $n = 3.3$ for both temperatures, hence an incipient contribution of diffusion mechanisms might be expected. Though the measured stress exponent did not drop as low, a progressive decrease in n with strain was observed at 1000 K.

Our measured grain sizes for 1000 K and high strain are also consistent with the paleopiezometer of Rutter (1995) and Schmid et al. (1980) and cover the interval between the two lines for migration and rotation recrystallization, respectively. The microstructure indicates both migration and rotation recrystallization at this temperature. We may interpret this coexistence in terms of cyclic dynamic recrystallization (Lloyd and Freeman, 1991, 1994). Grain boundary bulging and subgrain rotation would produce the smaller grains that later would grow by grain boundary migration until they got consumed and entered the cycle again.

At 1200 K, the higher experimental temperature initially favored fast migration of grain boundaries over subgrain rotation recrystallization. Though we did not analyze the impurity distribution nor measured boundary migration velocities, it appears from the microstructures at low strain that the boundary migration displacement at 1200 K was much larger than at 1000 K (compare Figs. 8b and 10b). This faster migration is interpreted to be related to the transition from 'impurity loaded' to 'free' migration as defined by Guillopé and Poirier (1979). At high strain, the recrystallized grain size is more homogeneous and fits with the line for rotation recrystallization.

According to the deformation mechanism map, the conditions for 1200 K are close to the grain size sensitive field with low stress exponent ($n = 1.7$). Hence, a transition to grain size sensitive creep with low n is more likely to occur at 1200 K than at 1000 K. Our results from the stepping strain rate tests at 1200 K do not show the expected low n values, presumably because the lower resolution limit of the torque cell was reached in the experiments.

6.3. Shape fabric and strain

Progressive shear deformation at both experimental temperatures is associated with the development of different types of SPO for the different grain size fractions. For the porphyroclasts, both aspect ratio and preferred orientation are closely related to the finite magnitude of the imposed

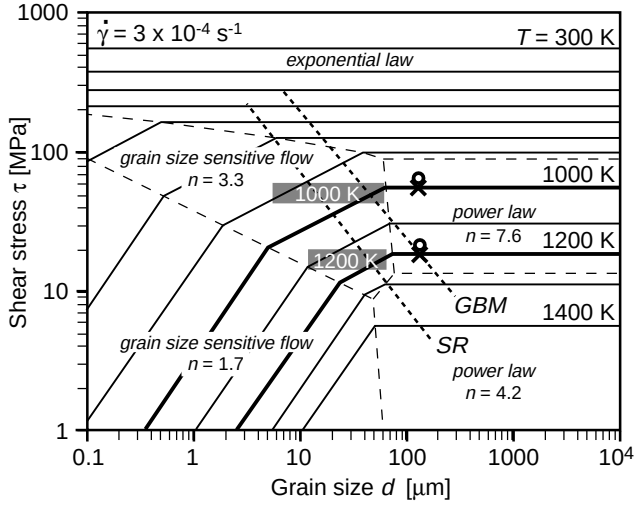

Fig. 14. Deformation mechanism map of calcite for constant shear strain rate of 3×10^{-4} s^{-1} with temperature contours at 100 K intervals (data after Schmid et al. (1980) and Walker et al. (1990)). The shear stresses predicted for the starting grain size (crosses) and peak stresses measured at low strain (circles) are marked. The gray bars represent the wide range in recrystallized grain sizes and steady-state flow stresses at high shear strain. Calcite paleopiezometers (short dashed lines) for subgrain rotation (SR) and grain boundary migration (GBM) recrystallization according to Rutter (1995) and Schmid et al. (1980).

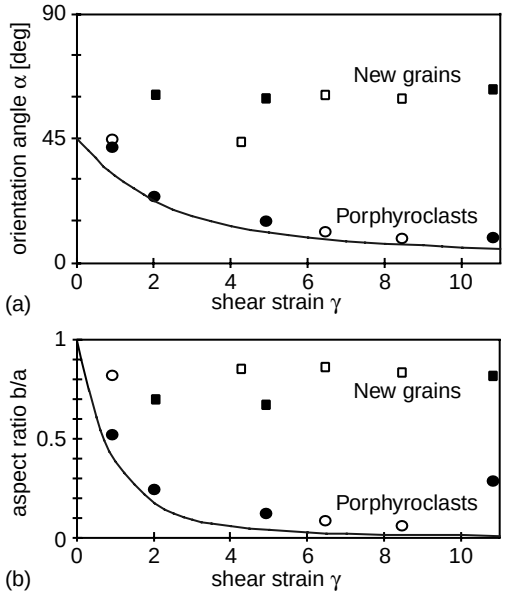

Fig. 15. (a) Grain shape preferred orientation angle α and (b) aspect ratio b/a for porphyroclasts (circles) and new grains (squares) with increasing shear strain. Tests at 1000 K (closed symbols) and 1200 K (open symbols). The curves represent the orientation angle, respectively, the aspect ratio of the theoretical strain ellipse as a function of γ.

bulk shear, resulting in largely stretched grains rotated towards the SZB. The newly recrystallized grains define an oblique SPO with preferred grain boundary alignment at about 60° with respect to the SZB and have only weakly elongate shapes.

The values for orientation angle and aspect ratio determined from the experiments are compared with the theoretical values of the finite strain ellipse assuming simple shear (Fig. 15). The porphyroclasts reflect the finite bulk strain, though their aspect ratio and preferred orientation are slightly behind the theoretical values calculated for the shear strain at the outer sample radius. This is mostly due to the fact that the actual amount of shear on the thin section surface is 10–20% less than that calculated. In contrast to the porphyroclasts, the SPO of the newly recrystallized grains deviates largely from that of the finite strain ellipse and attains steady-state shape and orientation at low (1000 K) to intermediate (1200 K) shear strain. The steady-state SPO in the recrystallized matrix at high strain ($\gamma > 5$) is similar for both temperatures.

The development of the two SPO types is a consequence of different mechanisms. The porphyroclasts SPO is due to intracrystalline deformation by dislocation glide within the original grains. With increasing strain, the relic grains are dissected by steep micro shears along defect concentrations, which favor the nucleation of new grains with grain boundaries aligned. This results in a secondary foliation, which is clearly visible in the microphotographs (Figs. 8g and 10g). It is mainly due to preferred alignment of steeply oriented grain boundaries rather than a strong elongation of the recrystallized grains. Such a steeply oriented foliation in newly recrystallized grains has also been observed in analog materials like norcamphor deformed in simple shear (Herwegh and Handy, 1998) and in natural mylonites (e.g. Brunel, 1980).

6.4. Processes of texture formation

At low strain, the LPO patterns from both experimental temperatures agree well with the deformation textures shown in previous work. Our A, B, and D orientations correspond, respectively, to *c*-axis maxima II, III and I of Schmid et al. (1987). The oblique LPO results from orientation B being preferred over A. The *c*-axis maximum I normal to the SZB (orientations D1/D2) with the basal plane parallel to the shear plane has been reported for the grain boundary migration regime and attributed to slip on $\{c\}\langle a\rangle$ (Schmid et al., 1987). At high strain most of the grains have assumed one of two single orientations (C1/C2), and there is no further texture evolution for increasing strain. Even though the microstructures are still evolving, the textural development seems to have reached a steady-state. The preferred orientation obtained at large shear strain is somehow puzzling because the crystals are aligned for 'easy slip' on $\{r\}\langle a\rangle$. This slip system $\{r\}\langle a\rangle$ has not been reported in calcite yet, but was inferred by Pieri et al. (2001) for three reasons. First, $\{r\}\langle a\rangle$ is a slip system in another carbonate (dolomite) at high temperature. Second, the *r*-plane and *a*-direction are common in calcite slip systems, just not reported in this combination. Third, simple shear deformation of calcite has been modeled with the self-consistent plasticity theory including a model for dynamic recrystallization. The numerical simulation reproduced the recrystallization texture very well if the $\{r\}\langle a\rangle$ slip systems is added to the conventional slip systems of calcite in a soft orientation recrystallization scenario.

6.5. Stages of microstructural evolution with strain

The microstructures of the specimens deformed at 1000 and 1200 K are different at low strain, but approach a similar mylonitic fabric at high strain for both temperatures. We identify three main stages of microstructural evolution with increasing shear strain (here specifically for 1000 K, Fig. 16).

$0 < \gamma < 2$: *Glide-induced vorticity stage—shear deformation microstructure*. This first deformation phase is characterized by homogeneous shearing and elongation of grains. Dislocation glide is the most important

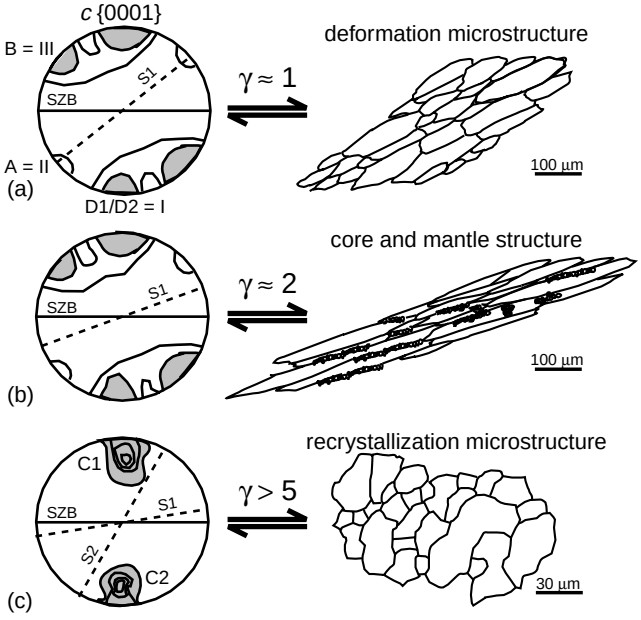

Fig. 16. Schematic *c*-axis distributions and grain shape fabrics for simple shear deformation at 1000 K. (a) *Deformation microstructure*: the *c*-axis maxima are slightly asymmetric with respect to the main foliation (S_1), and both are oblique with respect to the SZB. The roman numbers I, II and III represent the *c*-axis maxima defined by Schmid et al. (1987) and correspond to the ideal orientations A, B and D1/D2 of Fig. 13e. (b) *Transient core and mantle structure*: the LPO has changed little but the foliation (S_1) is closer to the SZB. The *c*-axis maxima are symmetrically disposed with respect to the foliation. (c) *Recrystallization microstructure*: the *c*-axis maxima are symmetric with respect to the SZB. The primary foliation (S_1) is close to the SZB, and a secondary foliation (S_2) has a large angle to both the SZB and LPO. The *c*-axis maxima C1/C2 of the recrystallization texture as defined in Fig. 13e are marked.

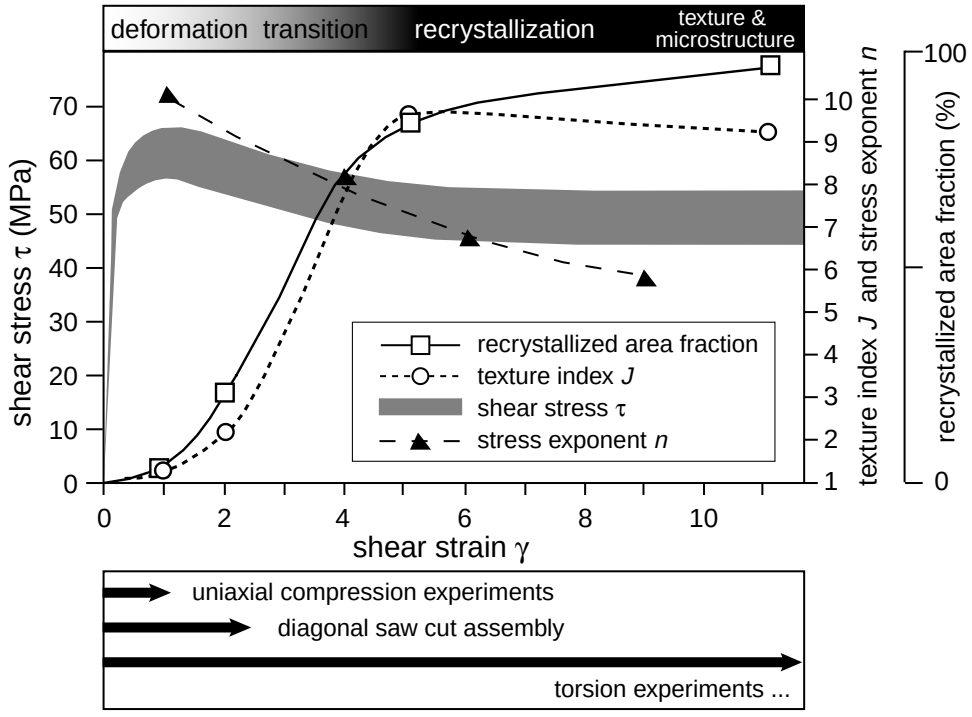

Fig. 17. Rheological, textural and microstructural evolution of Carrara marble deformed to high shear strain in torsion. Shear stress τ, stress exponent n, texture index J and area fraction of recrystallized grains given as function of shear strain γ. The strain intervals accessible in different types of experiments are indicated at the bottom.

strain-accommodating process. Grain boundary migration and subgrain rotation are minor. Bulging recrystallization occurs, but there are no fast migrating boundaries at this temperature. The LPO is the typical deformation texture, with *c*-axis maxima oblique and normal to the SZB.

$2 < \gamma < 5$: *Grain size reduction stage—transient core-and-mantle microstructure*. Incipient dynamic recrystallization induces a dramatic reduction in grain size by a combination of subgrain rotation and grain boundary migration. Subgrains first form near grain boundaries, resulting in a typical core-and-mantle microstructure. The LPO evolves towards the recrystallization texture with two single orientation components.

$5 < \gamma < 11$: *Steady-state stage—recrystallization microstructure*. At high shear strain, the rock is almost completely recrystallized to a homogeneously fine-grained aggregate. The microstructure is mainly determined by the recrystallization processes. A secondary foliation indicates the sense of shear, and the SPO does not change with further strain. The LPO is also strain invariant and forms a strong recrystallization texture, which consists of two single orientation components symmetric with respect to the SZB.

6.6. Fabric symmetry

The symmetry of SPO and LPO has often been used to determine the sense of shear in natural mylonites, where the absolute orientation of the shear kinematics (i.e. the SZB) is known only in rare cases (e.g. Bestmann et al., 2000). Analysis of our deformation experiments shows that the orientation of the SPO, LPO and SZB rotate with respect to each other with progressive strain (Fig. 16). At low strain, the SPO defined by the porphyroclasts (foliation S_1) relates in magnitude and direction to the imposed bulk shear and is oriented at an oblique angle to both the SZB and LPO. At medium strain, the LPO remains oblique relative to the SZB, but the SPO (S_1) rotates more towards the SZB while still at some oblique angle. The LPO and SPO are now nearly symmetrically disposed with respect to each other, and the small angle between the *c*-axis maxima and the primary foliation S_1 changes sign within a small strain increment. If the SZB had not been known, no sense of shear could have been derived. At high strain, the primary SPO (foliation S_1) tends to rotate into parallelism with the SZB. A secondary foliation (S_2) defined by preferred boundary alignment of the newly recrystallized grains is oriented at a large oblique angle to the SZB, and gives a good kinematic shear indication. The LPO alone does not give any information about the sense of shear, because the orientation maxima in the recrystallization texture are perfectly symmetrical with respect to SZB. As often applied for strain analysis of naturally deformed rocks (Ramsay and Huber, 1983), shape and orientation of the porphyroclasts can be used to quantify the imposed bulk shear for $\gamma < 5$, and becomes increasingly imprecise for higher shear strain.

6.7. When is steady-state reached?

One of the most significant results of this study is that the different rheological and microfabric characteristics attain steady-state at different shear strains. At 1000 K for example, the SPO of recrystallized grains is independent of strain for $\gamma > 2$, while steady-state flow stress, equilibrium grain size and stationary LPO are only reached somewhere between $2 < \gamma < 5$. The rheological and microstructural evolution of the specimens deformed at 1000 K is summarized in Fig. 17 where flow stress, texture index J, stress exponent n and the area fraction of recrystallized grains are plotted against the shear strain γ. Strain weakening correlates both with LPO development (geometrical softening) and grain size reduction (grain size sensitive flow). Therefore, it appears that a steady-state flow stress is not attained until the microstructure also reaches steady-state in terms of texture and grain size. While a few porphyroclasts may exist in a recrystallized matrix up to very high strain, mechanical steady-state is achieved when the recrystallized grains form an interconnected network separating deformed relics of the original grains from each other.

Per definition, true steady-state should establish irrespectively of the starting situation of the material, as long as the deformation conditions remain constant in time. Therefore, fine-grained and coarse-grained calcite aggregates should eventually arrive at the same state under equivalent external conditions. High strain torsion experiments were interpreted to have reached steady-state for both Solnhofen limestone (Casey et al., 1998) and Carrara marble (this study and Pieri et al., 2001). In common for both is a homogeneous fine grained microstructure of nearly equant grains, which no longer changes with progressive shear strain. Also in common for both is the development of a stationary LPO, with $\{r\}\langle a\rangle$ and $\{c\}\langle a\rangle$ preferred orientations and orthorhombic sample symmetry with respect to the kinematic reference frame. The texture is much weaker in the sheared limestone than in the deformed marble, possibly because more strain is accommodated by grain boundary sliding in the rather impure limestone. Without a detailed rheological comparison, the steady-state flow stresses compare reasonably well for both materials.[3] Keeping in mind some compositional differences between the marble and the limestone, all evidence indicates that they were approaching a common steady-state.

7. Summary and conclusions

The results of this study are summarized and lead to the following conclusions:

1. High temperature torsion experiments can attain simple shear geometry and reach shear strain magnitudes ($\gamma > 10$) of natural mylonites. Such experiments are useful to carefully monitor the influence of strain on rheology, microstructure and LPO and thus on deformation mechanisms and localization processes.
2. Carrara marble goes through complex changes in both rheology and microstructure as it deforms to high shear strain within the dislocation creep regime. Diffusion processes start to contribute to the deformation only when a large fraction of the marble has recrystallized to a fine grain size.
3. Strain weakening is associated both with recrystallization to a fine grain size and with the development of a strong LPO. Steady-state stress is achieved when the relic coarse grains become isolated and the fine grained matrix becomes the stress supporting framework.
4. Carrara marble shows a profound LPO development for finite shear up to γ of 5–8, then remains stationary for higher strain with a preferred orientation aligned for easy slip on $\{r\}\langle a\rangle$. This slip system $\{r\}\langle a\rangle$ has been proposed as an additional slip system in calcite at high temperatures. The strain at which a steady-state LPO is established increases with temperature and is in good correlation with the formation of a steady-state recrystallization microstructure.
5. The shear sense in medium strained marbles can only be determined if the SZB is exposed, because the LPO is nearly perpendicular to the SPO (foliation S_1), and both are at similarly oblique angles to the SZB. At high strain, the angle between the two foliations S_1 and S_2 gives direct information on the shear sense even without prior knowledge of the shear kinematics (SZB).
6. The concept of steady-state is difficult to define because not all microstructural elements become strain invariant simultaneously. It requires much higher strain than previously assumed to establish a true steady-state.

Acknowledgements

This work is a result of projects no. 2100-045646.95 and 2000-052494.97 of the Swiss National Fonds. We thank Jean-Pierre Burg (Zürich) for initiating and continuously supporting this study. Mervyn S. Paterson (Canberra) is particularly thanked for design and construction of the torsion apparatus and for most helpful discussions. Renee Heilbronner (Basel) and Marco Herwegh (Bern) introduced us into the SPO analysis programs. Massimo Coli (Firenze) gave assistance to select the block of marble in the Lorano quarry. This paper largely benefited from constructive criticism by Stefan Schmid (Basel) as well as from discussions with Ernest Rutter (Manchester), Michel Bestmann (Erlangen) and Auke Barnhoorn (Zürich). Comments from an anonymous reviewer are acknowledged. MP received a

[3] Solnhofen limestone was deformed at 1023 K (750°C) and 10^{-3} s^{-1} and flows under a torque of 39 Nm, which corresponds to a shear stress of 60 (50) MPa at the outer radius assuming $n = 1$ (3) after Eq. (4).

stipendium provided by ETH Zürich to complete this manuscript.

References

Adams, B.L., Wright, S.I., Kunze, K., 1993. Orientation imaging: the emergence of a new microscopy. Metallurgical Transactions A (Physical Metallurgy and Materials Science) 24A (4), 819–831.

Bestmann, M., Kunze, K., Matthews, A., 2000. Evolution of a calcite marble shear zone complex on Thassos Island, Greece: microstructural and textual fabrics and their kinematic significance. Journal of Structural Geology 22 (11–12), 1789–1807.

Bons, P.D., Jessell, M.W., 1999. Micro-shear zones in experimentally deformed octachloropropane. Journal of Structural Geology 21 (3), 323–334.

Brunel, M., 1980. Quartz fabrics in shear-zone mylonites; evidence for a major imprint due to late strain increments. Tectonophysics 64 (3–4), T33–T44.

Carmignani, L., Giglia, G., Kligfield, R., 1978. Structural evolution of the Apuane Alps; an example of continental margin deformation in the northern Apennines, Italy. Journal of Geology 86 (4), 487–504.

Carmignani, L., Klingfield, R., 1990. Crustal extension in the Northern Apennines: the transition form compression to extension in the Alpi Apuane core complex. Tectonics 9, 1275–1303.

Casey, M., Kunze, K., Olgaard, D.L., 1998. Texture of Solnhofen Limestone deformed to high strains in torsion. Journal of Structural Geology 20 (2–3), 255–267.

Coli, M., 1989. Times and mode of uplift of the Apuane Alps metamorphic complex. Atti Ticinensi di Scienze della Terra 32, 47–56.

Dell Angelo, L.N., Tullis, J., 1996. Textural and mechanical evolution with progressive strain in experimentally deformed aplite. Tectonophysics 256 (1–4), 57–82.

Etheridge, M.A., Wilkie, J.C., 1979. Grainsize reduction, grain boundary sliding and the flow strength of mylonites. Tectonophysics 58 (1–2), 159–178.

Guillopé, M., Poirier, J.P., 1979. Dynamic recrystallization during creep of single-crystalline halite; an experimental study. Journal of Geophysical Research 84 (B10), 5557–5567.

Handin, J.W., Higgs, D.V., O, B.J.K., 1960. Torsion of Yule marble under confining pressure. In: Griggs, D.T. (Ed.). Rock Deformation—A Symposium. Memoir–Geological Society of America 79. Geological Society of America (GSA), Boulder, CO, USA, pp. 245–274.

Handin, J., Heard, H.C., Magouirk, J.N., 1967. Effects of the intermediate principal stress on the failure of limestone, dolomite, and glass at different temperatures and strain rates. Journal of Geophysical Research 72 (2), 611–640.

Herwegh, M., Handy, M.R., 1998. The origin of shape preferred orientations in mylonite; inferences from in situ experiments on polycrystalline norcamphor. Journal of Structural Geology 20 (6), 681–694.

Jessell, M.W., Lister, G.S., 1991. Strain localization behaviour in experimental shear zones. Pure and Applied Geophysics 137 (4), 421–438.

Leiss, B., Ullemeyer, K., Weber, K., Passchier, C., 2000. Textures and Physical Properties of Rocks. Journal of Structural Geology 22 (11/12), 1527–1873.

Lloyd, G.E., Freeman, B., 1991. SEM electron channelling analysis of dynamic recrystallization in a quartz grain. Journal of Structural Geology 13 (8), 945–953.

Lloyd, G.E., Freeman, B., 1994. Dynamic recrystallization of quartz under greenschist conditions. Journal of Structural Geology 16 (6), 867–881.

Molli, G., Conti, P., Giorgetti, G., Meccheri, M., Oesterling, N., 2000. Microfabric study on the deformational and thermal history of the Alpi Apuane marbles (Carrara marbles), Italy. Journal of Structural Geology 22, 1809–1825.

Panozzo, R.H., 1983. Two-dimensional analysis of shape-fabric using projections of digitized lines on a plane. Tectonophysics 95 (3–4), 279–294.

Panozzo, R.H., 1984. Two-dimensional strain from the orientation of lines in a plane. Journal of Structural Geology 6 (1–2), 215–221.

Paterson, M.S., Olgaard, D.L., 2000. Rock deformation tests to large shear strains in torsion. Journal of Structural Geology 22 (9), 1341–1358.

Pieri, M., Kunze, K., Burlini, L., Stretton, I., Olgaard, D.L., Burg, J.-P., Wenk, H.-R., 2001. Texture development of calcite by deformation and dynamic recrystallization at 1000 K during torsion experiments of marble to large strains. Tectonophysics 330 (1–2), 119–140.

Prior, D.J., Boyle, A.P., Brenker, F., Cheadle, M.C., Day, A., Lopez, G., Peruzzo, L., Potts, G., Reddy, S., Spiess, R., Timms, N.E., Trimby, P., Wheeler, J., Zetterstrom, L., 1999. The application of electron backscatter diffraction and orientation contrast imaging in the SEM to textural problems in rocks. American Mineralogist 84 (11–12), 1741–1759.

Ramsay, J.G., Huber, M.I., 1983. The Techniques of Modern Structural Geology. Academic Press, London.

Rutter, E.H., 1995. Experimental study of the influence of stress, temperature, and strain on the dynamic recrystallization of Carrara Marble. Journal of Geophysical Research, B, Solid Earth and Planets 100 (12), 24,651–24,663.

Rutter, E.H., 1998. Use of extension testing to investigate the influence of finite strain on the rheological behaviour of marble. Journal of Structural Geology 20 (2–3), 243–254.

Rutter, E.H., 1999. On the relationship between the formation of shear zones and the form of the flow law for rocks undergoing dynamic recrystallization. Tectonophysics 303 (1–4), 147–158.

Rutter, E.H., Casey, M., Burlini, L., 1994. Preferred crystallographic orientation development during the plastic and superplastic flow of calcite rocks. Journal of Structural Geology 16 (10), 1431–1446.

Schmid, S.M., 1982. Microfabric studies as indicators of deformation mechanisms and flow laws operative in mountain building. In: Hsue, K.J. (Ed.). Mountain Building Processes. Academic Press, London, UK, pp. 95–110.

Schmid, S.M., Boland, J.N., Paterson, M.S., 1977. Superplastic flow in finegrained limestone. Tectonophysics 43 (3–4), 257–291.

Schmid, S.M., Paterson, M.S., Boland, J.N., 1980. High temperature flow and dynamic recrystallization in Carrara Marble. Tectonophysics 65 (3–4), 245–280.

Schmid, S.M., Panozzo, R., Bauer, S., 1987. Simple shear experiments on calcite rocks; rheology and microfabric. Journal of Structural Geology 9 (5–6), 747–778.

Tullis, J., Yund, R.A., 1982. Grain growth kinetics of quartz and calcite aggregates. Journal of Geology 90 (3), 301–318.

Urai, J.L., Means, W.D., Lister, G.S., 1986. Dynamic recrystallization of minerals. In: Hobbs, B.E., Heard, H.C. (Eds.). Mineral and Rock Deformation; Laboratory Studies; The Paterson Volume. American Geophysical Union, Washington, DC, USA, pp. 161–199.

Walker, A.N., Rutter, E.H., Brodie, K.H., 1990. Experimental study of grain-size sensitive flow of synthetic, hot-pressed calcite rocks. In: Knipe, R.J., Rutter, E.H. (Eds.). Deformation Mechanisms, Rheology and Tectonics. Geological Society Special Publications 54. Geological Society of London, London, UK, pp. 259–284.

Wenk, H.R., Venkitasubramanyan, C.S., Baker, D.W., Turner, F.J., 1973. Preferred orientation in experimentally deformed limestone. Contributions to Mineralogy and Petrology 38 (2), 81–114.

Wenk, H.R., Matthies, S., Donovan, J., Chateigner, D., 1998. BEARTEX, a Windows-based program system for quantitative texture analysis. Journal of Applied Crystallography 31, 262–269.

White, S.H., Burrows, S.E., Carreras, J., Shaw, N.D., Humphreys, F.J., 1980. On mylonites in ductile shear zones. Journal of Structural Geology 2 (1/2), 175–187.

Zhang, S., Karato, S.I., 1995. Lattice preferred orientation of olivine aggregates deformed in simple shear. Nature 375 (6534), 774–777.